

# The Richness-to-Mass Relation of CAMIRA Galaxy Clusters from Weak-lensing Magnification in the Subaru Hyper Suprime-Cam Survey

I-Non Chiu<sup>1</sup>, Keiichi Umetsu<sup>1</sup>, Ryoma Murata<sup>2,3</sup>, Elinor Medezinski<sup>4</sup>, Masamune Oguri<sup>2,3,5</sup>

<sup>1</sup> Academia Sinica Institute of Astronomy and Astrophysics (ASIAA), 11F of AS/NTU Astronomy-Mathematics Building, No.1, Sec. 4, Roosevelt Rd, Taipei 10617, Taiwan

<sup>2</sup> Kavli Institute for the Physics and Mathematics of the Universe (WPI), The University of Tokyo Institutes for Advanced Study (UTIAS), The University of Tokyo, 5-1-5 Kashiwanoha, Kashiwa-shi, Chiba, 277-8583, Japan

<sup>3</sup> Department of Physics, University of Tokyo, 7-3-1 Hongo, Bunkyo-ku, Tokyo 113-0033 Japan

<sup>4</sup> Department of Astrophysical Sciences, Princeton University, Princeton, NJ 08544, USA

<sup>5</sup> Research Center for the Early Universe, University of Tokyo, Tokyo 113-0033, Japan

19 May 2022

## ABSTRACT

We present a statistical weak-lensing magnification analysis on an optically selected sample of 3029 CAMIRA galaxy clusters with richness  $N > 15$  in the Subaru Hyper Suprime-Cam (HSC) survey. The CAMIRA sample spans a wide redshift range of  $0.2 \leq z < 1.1$ . We use two distinct populations of color-selected, flux-limited background galaxies, namely the low- $z$  and high- $z$  samples at mean redshifts of  $\approx 1.1$  and  $\approx 1.4$ , respectively, from which to measure the weak-lensing magnification signal by accounting for cluster contamination as well as masking effects. Our magnification bias measurements are found to be uncontaminated according to validation tests against the “null-test” samples for which the net magnification bias is expected to vanish. The magnification bias for the full CAMIRA sample is detected at a significance level of  $8.29\sigma$ , which is dominated by the high- $z$  background. We forward-model the observed magnification data to constrain the richness-to-mass ( $N$ – $M$ ) relation for the CAMIRA sample. In this work, we can only constrain the normalization of the  $N$ – $M$  relation by employing informative priors on the mass and redshift trends, and on the intrinsic scatter at fixed mass. The resulting scaling relation is  $N \propto M_{500}^{0.91 \pm 0.14} (1+z)^{-0.45 \pm 0.75}$ , with a characteristic richness of  $N = (19.63 \pm 3.16)$  and intrinsic log-normal scatter of  $0.14 \pm 0.07$  at  $M_{500} = 10^{14} h^{-1} M_{\odot}$ . With the derived  $N$ – $M$  relation, we provide magnification-calibrated mass estimates of individual CAMIRA clusters, with the typical uncertainty of  $\approx 38\%$  and  $\approx 30\%$  at richness  $\approx 20$  and  $\approx 40$ , respectively. We further compare our magnification-inferred  $N$ – $M$  relation with those from the shear-based results in the literature, finding good agreement.

**Key words:** galaxies: clusters: lensing: magnification: scaling relations

## 1 INTRODUCTION

Galaxy clusters, as local peaks of cosmic density perturbations, are powerful cosmological tools because they provide a representative view of nonlinear growth of structure over cosmic time. Cosmological probes based on galaxy clusters enable independent tests to examine any viable cosmological models and constrain fundamental properties of the universe, such as the amplitude of cosmic inhomogeneity, the growth of cosmic structure, and the equation of state of dark energy (e.g., Wang & Steinhardt 1998; Holder et al. 2001). Measurements of the cluster abundance as a function of redshift in large cluster surveys have been used in cosmological studies with promising success (Benson et al. 2013; Planck Collaboration et al. 2015; Bocquet et al. 2015; de Haan et al. 2016; Bocquet et al. 2018), demonstrating that the constraining power of galaxy clusters

is as competitive as other complementary probes, such as observations of the cosmic microwave background (CMB) and the large-scale clustering of galaxies. However, one of the most substantial limitations of utilizing galaxy clusters as a feasible cosmological tool is to obtain an accurate and precise observable-to-mass scaling relation. This is because the cluster mass is not directly observable and must be inferred from a mass proxy—an observed quantity that is well correlated with the underlying cluster mass.

Various observable properties of galaxy clusters can be used as a mass proxy, such as the X-ray luminosity and temperature due to the Bremsstrahlung emission from the hot intra-cluster medium (ICM). In the context of cluster galaxy populations, the richness  $N$ —the overdensity of red-sequence galaxies—is often used as a mass proxy for galaxy clusters selected in optical imaging sur-

veys. Although optical richness serves as a low-scatter mass proxy (Rykoff et al. 2012), an unbiased calibration of the cluster mass is needed to accurately anchor the richness-to-mass ( $N$ – $M$ ) scaling relation. With the goal of achieving an accurate mass calibration, a number of observational approaches are available, including those based on the velocity dispersion of member galaxies (Saro et al. 2013), the dynamical Jeans analysis (Capasso et al. 2019b,a), X-ray observations assuming hydrostatic equilibrium (Vikhlinin et al. 2006, 2009; Martino et al. 2014), weak gravitational lensing (hereafter weak lensing; Umetsu et al. 2014; von der Linden et al. 2014; Hoekstra et al. 2015; Melchior et al. 2017; Dietrich et al. 2019; McClintock et al. 2019; Murata et al. 2018), and so on. Among all these probes, weak lensing is regarded as the most direct approach to calibrating the cluster mass with near zero bias, because it is free from any assumption about the dynamical state of clusters and is only sensitive to the underlying mass distribution. Accordingly, weak lensing has been extensively used as a direct mass probe for cosmological studies, albeit with large scatter (Mantz et al. 2015; Grandis et al. 2018; Bocquet et al. 2018).

Gravitational lensing due to mass inhomogeneities along the line of sight deflects light from distant background sources, resulting in various observable effects, such as strong lensing, weak-lensing shear, and weak-lensing magnification. The weak shear effect introduces a small but coherent change in the observed ellipticities of background images. The effect of lensing magnification enlarges (reduces) the observed solid angle on the sky, which results in an increase (decrease) of the total flux of background sources (for more details, see Bartelmann & Schneider 2001).

Over the last two decades, tremendous efforts have been made to standardize the weak shear effect as a reliable mass calibrator through systematic observing campaigns (e.g., von der Linden et al. 2014; Umetsu et al. 2014; Hoekstra et al. 2015; Okabe & Smith 2016; Sereno et al. 2017; Stern et al. 2018; Dietrich et al. 2019; Miyatake et al. 2019), with an aid of intensive image simulations (Massey et al. 2007; Bridle et al. 2010; Mandelbaum et al. 2015; Hoekstra et al. 2017). On the other hand, there have been relatively less attempts on using lensing magnification for cluster mass measurements, which is mainly due to the fact that the signal-to-noise ratio of magnification measurements is significantly less than those from shear-based measurements (Schneider et al. 2000). Although the signal-to-noise ratio of lensing magnification is low on an individual cluster basis, stacking a sizable sample of galaxy clusters allows us to overcome this problem, providing a precise mass calibration. It is worth emphasizing that this stacking strategy is becoming progressively valuable and competitive because of ongoing and forthcoming large cluster surveys (e.g., the Dark Energy Survey; DES Collaboration 2005), as demonstrated in recent studies of CMB cluster lensing (e.g., Baxter et al. 2018) and dynamical analysis (e.g., Capasso et al. 2019a). Alternatively, lensing magnification can be used in combination with weak lensing shear to perform a joint reconstruction of the cluster mass distribution (Schneider et al. 2000; Umetsu & Broadhurst 2008; Umetsu 2013; Umetsu et al. 2018; Chiu et al. 2018b), effectively breaking degeneracies inherent in a standard shear-only analysis (Bartelmann & Schneider 2001).

Recently, high signal-to-noise measurements of lensing magnification have been obtained by stacking over large cluster samples, from which to calibrate the cluster mass with better precision and accuracy (e.g., Hildebrandt et al. 2009; Ford et al. 2012, 2014; Chiu et al. 2016a). In contrast to the standard shear-based analysis, measuring the effect of lensing magnification does not require source galaxies to be spatially resolved. However, it does require

accurate photometry and a stringent flux limit against incompleteness effects (Umetsu 2013). Hence, lensing magnification has been extended to measure the mass of galaxy clusters at high redshift ( $z \approx 1.4$ ; Tudorica et al. 2017), for which the shape measurement of faint source galaxies required by shear-based methods is extremely challenging with ground-based observations. In this context, lensing magnification is unique and attractive for mass calibration of galaxy clusters at high redshift, especially for ongoing and upcoming wide and deep lensing surveys.

In this study, we aim to extract the lensing magnification signal around a large statistical sample of optically selected galaxy clusters from the ongoing Hyper Suprime-Cam (HSC) survey (Aihara et al. 2018a). We then calibrate the cluster mass scale of the selected sample over a wide range of richness and redshift using lensing magnification alone. Here we focus on the effects of “flux magnification bias” (see more details in Section 2), where we extend the approach of Chiu et al. (2016a). Specifically, we select two distinct populations of background galaxies behind the clusters in color-color space and measure their projected number density contrast relative to random fields. The most notable improvement over the previous work is that we use a forward-modelling approach (Section 5.6) to jointly constrain the underlying observable-to-mass relation, namely the  $N$ – $M$  relation.

This paper is organized as follows. A brief overview of cluster lensing magnification is given in Section 2. Section 3 describes the HSC survey and data. The cluster sample we use is described in Section 4. We detail the analysis of lensing magnification and the mass calibration procedures in Section 5. We present our results in Section 6. Discussion of systematic uncertainties is given in Section 7. Finally, a summary and conclusions are provided in Section 8.

Throughout this paper, we assume a flat  $\Lambda$ CDM cosmology with  $\Omega_M = 0.3$ ,  $H_0 = h \times 100 \text{ km s}^{-1} \text{ Mpc}^{-1}$  with  $h = 0.7$ , and  $\sigma_8 = 0.8$ , the rms amplitude of linear mass fluctuations in a sphere of comoving radius  $8h^{-1} \text{ Mpc}$ . We adopt the standard notation  $M_{500}$  to denote the mass enclosed within a sphere of radius  $R_{500}$  within which the mean overdensity equals to 500 times the critical density  $\rho_c(z)$  of the universe at the cluster redshift. Unless otherwise stated, all quoted errors represent the 68% confidence level (i.e.,  $1\sigma$ ). We use the AB magnitude system in photometry. The notation  $\mathcal{N}(x, y^2)$  stands for a normal distribution with the mean  $x$  and the standard deviation  $y$ .

## 2 THE BASICS OF GRAVITATIONAL LENSING

A brief review of gravitational lensing, with emphasis on the weak lensing effect of magnification bias around galaxy clusters, is provided in this section. For more details, we refer the reader to Bartelmann & Schneider (2001), Umetsu (2011) and Hoekstra et al. (2013).

In the limit of thin lens approximation, a galaxy cluster at redshift  $z_l$  is considered as a single lens embedded in a homogeneous universe where background sources behind the cluster are all gravitationally lensed. To the first order, the true and observed angular positions of the source, denoted by  $\vec{\beta}$  and  $\vec{\theta}$  at the source and observed planes, respectively, can be related to each other by the lensing Jacobian matrix  $J$ , defined by

$$J(\vec{\theta}) \equiv \frac{\partial \vec{\beta}}{\partial \vec{\theta}} = \begin{pmatrix} 1 - \kappa - \gamma_1 & -\gamma_2 \\ -\gamma_2 & 1 - \kappa + \gamma_1 \end{pmatrix}, \quad (1)$$

where  $\kappa$ ,  $\gamma_1$ , and  $\gamma_2$  are linear combinations of second derivatives of

the effective lensing potential. The lensing convergence,  $\kappa(\vec{\theta})$ , is a dimensionless version of the projected surface mass density  $\Sigma_m(\vec{\theta})$ , defined by

$$\kappa(\vec{\theta}) = \frac{\Sigma_m(\vec{\theta})}{\Sigma_c}, \quad (2)$$

where  $\Sigma_c$  is the critical surface density defined as  $\Sigma_c \equiv \frac{c^2}{4\pi G} \frac{D_s}{D_l D_{ls}}$ , which depends on the angular diameter distances of the observer-to-cluster ( $D_l$ ), observer-to-source ( $D_s$ ), and the cluster-to-source ( $D_{ls}$ ) pairs, respectively;  $G$  is the Newton's constant, and  $c$  is the speed of light.

In the subcritical-lensing regime, lensing magnification changes the flux of background sources by a factor of  $\mu$ , where  $\mu$  is the inverse determinant of the Jacobian matrix:

$$\mu = \frac{1}{(1 - \kappa)^2 - |\gamma|^2}. \quad (3)$$

Hence, the observed surface density of the sources above a flux threshold increases because of flux amplification. On the other hand, magnification also reduces the observed area on the source plane given a solid angle, such that the surface number density of sources given an observed solid angle is effectively decreased. As a result, lensing magnification alters the surface number density of a “flux-limited” sample of background sources. Moreover, the net change depends on the intrinsic slope of the source luminosity function. This change in number counts caused by gravitational lensing is known as magnification bias (Broadhurst et al. 1995; Taylor et al. 1998; Umetsu 2013).

The effect of magnification bias can be measured using cumulative number counts of a flux-limited sample of background galaxies. Assuming that the luminosity function of background galaxies can be locally approximated by a power-law function of flux around the flux limit, the magnification bias can be described by

$$\frac{n_d(< m)}{n_0(< m)} = \mu^{\alpha-1}, \quad (4)$$

where  $n_d(< m)$  is the lensed surface number density of background galaxies that are brighter than the magnitude limit  $m$ ,  $n_0(< m)$  is its unlensed version, and  $\alpha$  is the logarithmic count slope,

$$\alpha \equiv 2.5 \frac{d \log n_0(< m)}{dm}.$$

In the weak-lensing limit ( $\kappa \ll 1$  and  $|\gamma| \ll 1$ ), equation (4) reduces to

$$\frac{n_d(< m)}{n_0(< m)} - 1 \approx 2(\alpha - 1)\kappa. \quad (5)$$

In the case of  $\alpha > 1$ , lensing magnification results in a net enhancement of the number density, and vice versa. When  $\alpha = 1$ , lensing magnification gives no net change in the source counts, even though background galaxies are magnified. This is because the depletion of source counts due to geometric expansion of the observed sky is in balance with the increase of source counts due to flux amplification. It should be noted that we use equation (4) without assuming the weak-lensing limit when interpreting the observed magnification profiles with the standard halo modeling (equation (19)).

To summarize, we can constrain the lensing convergence  $\kappa$ , and thus the cluster mass, by measuring the number density contrast of background galaxies with respect to random fields, once the unlensed count slope  $\alpha(m)$  as a function of the limiting magnitude  $m$  is known. It is worth stressing again that this method does not require source galaxies to be fully resolved, thus providing an

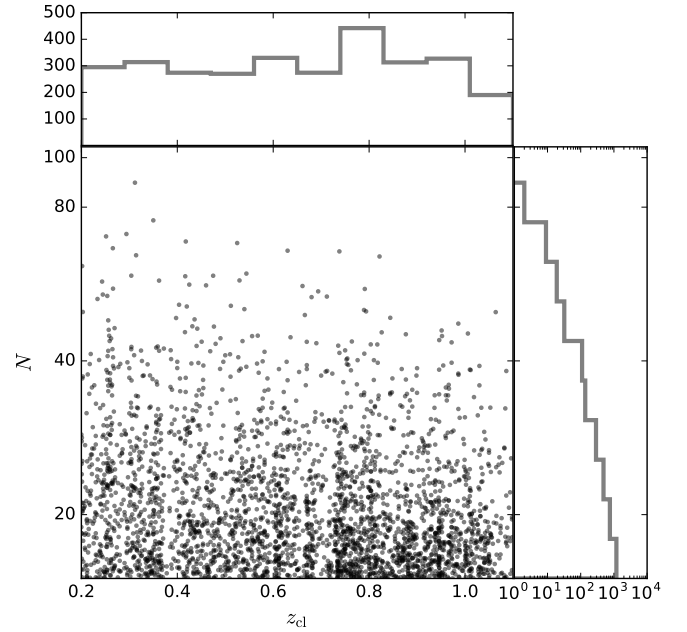


**Figure 1.** The cluster sample with  $N \geq 15$  at redshift  $0.2 \leq z < 1.1$  used in this work. In total, there are 3029 clusters. The photometric redshift and the richness of the clusters are shown in the x- and y-axis, respectively. The histograms of the richness and redshift are presented in the right and upper panels, respectively.

independent way to calibrate the cluster mass, complementary to the standard shear-based method.

### 3 DATA

We use the optical photometry obtained from the Hyper Suprime-Cam (HSC) Survey (Aihara et al. 2018a), which is carried out in the framework of a Subaru Strategic Program (SSP) using the newly installed wide-field camera Hyper Suprime-Cam (Miyazaki 2015) on the 8.2 m Subaru Telescope. A brief summary of the HSC survey is given below, and we refer the reader to Aihara et al. (2018a) for more details.

The HSC SSP is a five-year mission initialized in 2014 to survey a large sky area of  $1400 \text{ deg}^2$  in five broadband filters (*grizy*), with the goal of performing state-of-the-art weak lensing studies preparing for the era of the Large Synoptic Survey Telescope (LSST; Ivezić et al. 2008). The HSC survey is composed of three layers: Wide, Deep and UltraDeep. We only use data from the Wide layer in this work, because it is designed to cover the area of  $1400 \text{ deg}^2$  that is significantly larger than the Deep ( $\approx 25 \text{ deg}^2$ ) and UltraDeep ( $\approx 3.5 \text{ deg}^2$ ) layers. The exposure time of the full depth in the Wide layer is 10 (20) min for *g*- and *r*-band (*i*-, *z*-, and *y*-band). The 5 sigma limiting magnitudes around a  $2''$  aperture are 26.5 mag, 26.1 mag, 25.9 mag, 25.1 mag, and 24.4 mag for *g*-, *r*-, *i*-, *z*-, and *y*-band, respectively. As a result, this represents the deepest optical multi-band survey over an area of more than one thousand square degrees to date. This unique combination of area and depth enables us to search for and characterize galaxy clusters out to a redshift of  $z \approx 1$  or beyond with an unprecedented statistical power. In particular, the imaging of *i*-band is specifically taken under the good seeing condition ( $< 0.8''$ ), resulting in a mean

seeing of  $0.58''$  (Mandelbaum et al. 2018), which is excellent for weak-lensing studies, by design.

The imaging reduction and catalog construction of the HSC survey are processed by the `hscPipe` v5.4 (Bosch et al. 2018), a precursor pipeline of the data reduction and management for the LSST survey (Axelrod et al. 2010; Juric & Tyson 2015). Details of the `hscPipe` are fully given in Bosch et al. (2018), and we only briefly summarize the key steps, as follows.

The source detection and cataloging are carried out in two phases. In the first phase, `hscPipe` processes the single-epoch images in each band, involving several basic reductions, such as applying the flat-fielding correction and removing signatures of instrumental defects, followed by the initial calibration of astrometrics, photometry and the Point Spread Function (PSF) using the bright sources only. In the second phase, the source detection is performed on the coadd images, and the photometry is measured using the “forced” mode with the *i*-band as the reference band. The `cmodel` photometry (Lupton et al. 2001), which is the model-fitting photometry estimated by a composite template of an exponential profile and a de Vaucouleurs profile convolving with the locally registered PSF, is used in this work. The performance of the `cmodel` photometry has been intensively verified in Huang et al. (2018), showing that it can robustly deliver the unbiased estimates of color and magnitude for galaxies. Since our analysis does not include the cluster cores, we do not use the PSF-matched aperture photometry, which is designed to improve the estimation of colors in extremely crowded fields. More discussion about the PSF-matched aperture photometry can be found in Aihara et al. (2018b).

The bright star masks with the version of `Arcturus` are applied, as described in Coupon et al. (2018). We only apply the star masks in the *i*- and *z*-bands. The flag of `i_extendedness_value == 1` is applied to separate galaxies from stars. To construct the Full-Depth-Full-Color (FDFC) catalog, we apply the flags of `g[x]countinputs ≥ 4` and `i[zy]countinputs ≥ 6`. We further apply a magnitude cut in the *z*-band by the flag of `z_cmodel_mag - a_z < 26` to remove the extremely faint objects, which do not have reliable photometry measurements and are not of interest in this work; we have confirmed that this cut does not affect our magnification measurements. Similar to Oguri et al. (2018), we also apply the quality cuts to discard the objects whose photometry measurements are severely affected by the defected pixels or cosmic rays. A summary of the `sql` query is given in Table A1.

The HSC survey is planned to be completed by the end of 2019. There are three Public Data Release (PDR) for the HSC survey: The first PDR took place in February 2017 (Aihara et al. 2018b), containing the initial FDFC footprint of an area of  $\approx 140 \text{ deg}^2$ . The second and third PDR are scheduled to be in 2019 and 2021, respectively. In this work, we use the FDFC data taken up to 2017 (s17A) with an area of  $\approx 380 \text{ deg}^2$  (excluding the star-masked regions).

#### 4 CLUSTER SAMPLE

In this work, the galaxy clusters are identified using the CAMIRA algorithm (Cluster finding Algorithm based on Multi-band Identification of Red-sequence gALaxies; Oguri 2014). We summarize the CAMIRA algorithm as follows, and refer the reader to Oguri (2014) and Oguri et al. (2018) for more details.

CAMIRA is a matched-filter cluster finder to search for the over-density of red-sequence galaxies based on the stellar population

synthesis model, which is calibrated against a sample of spectroscopically observed galaxies. Each identified cluster is assigned with a photometric redshift estimate with accuracy better than 1% and a mass proxy of richness ( $N$ ) that is well correlating with the underlying cluster mass (Oguri et al. 2018). We use the cluster catalog produced by the CAMIRA, which is run on the s17A FDFC footprint with an area of  $\approx 380 \text{ deg}^2$  excluding the star-masked regions. This results in a sample of 3029 clusters with  $N \geq 15$  at redshift of  $0.2 \leq z < 1.1$ . Figure 1 shows the cluster sample we use in this work.

We use the location of the Brightest Cluster Galaxy (BCG) as the cluster center. Using a subset of clusters with available X-ray imaging, the center offset between the BCG and the X-ray peak is generally small ( $\lesssim 0.1 \text{ Mpc/h}$ ) with a long tail toward the high offset, suggesting that miscentering is not significant (Oguri et al. 2018). Moreover, lensing magnification is probing the surface mass density  $\Sigma$ , instead of the differential surface mass density  $\Delta\Sigma$ , thus is less sensitive to the miscentering effect (Ford et al. 2014; Ford & VanderPlas 2016). Therefore, we ignore the miscentering effect in this work.

We use the photometric redshift estimation ( $z_{cl}$ ) for each cluster, even for those clusters with available spectroscopic redshift  $z_{spec}$ , in the interest of uniformity. With the HSC data, the performance of photometric redshift is excellent: the bias, scatter, and the outlier rate of  $(z_{cl} - z_{spec})/(1 + z_{spec})$  are  $-0.0013$ ,  $0.0081$ , and  $1.7\%$ , respectively (Oguri et al. 2018). Given this quality, hereafter we ignore the photometric redshift uncertainty, which has negligible impact on the final result.

#### 5 ANALYSIS

Our goal is to characterize the  $N$ - $M$  scaling relation given the observables of the clusters. For each cluster, we have two observables: the richness  $N$  and the observed magnification profile. The richness  $N$  is estimated by the CAMIRA algorithm (see Section 4). In what follows, we will detail the extraction of the magnification profile for each cluster and the modelling of the  $N$ - $M$  scaling relation.

##### 5.1 Background Selection

We apply a color-color selection to obtain the background galaxies as the source sample used in this work. This selection is made in the color-color space of  $g-i$  vs  $r-z$ , for which this combination of colors has been demonstrated as an efficient way to deliver a sample of background galaxies with high purity (Medezinski et al. 2018). This color-color combination is designed to remove the foreground and cluster galaxies based on the synthetic evolutionary tracks of various types of galaxies in the color-color space (Medezinski et al. 2010). Interested readers are referred to Medezinski et al. (2018) for more details.

In this work, the color-color cuts are defined with the guidance from

- (i) the distribution of the cluster galaxies, and
- (ii) the redshift distribution among the color-color cells,

in the space of  $g-i$  vs  $r-z$ . The former can be derived as follows. First, we stack the distribution of the galaxies that lie projected within the clustercentric radius of  $0.5 \text{ Mpc}$  around the clusters in the  $g-i$  vs  $r-z$  space. Second, we also derive the reference distribution by carrying out the same stacking process on the random fields, and subtract the reference distribution from the stacked



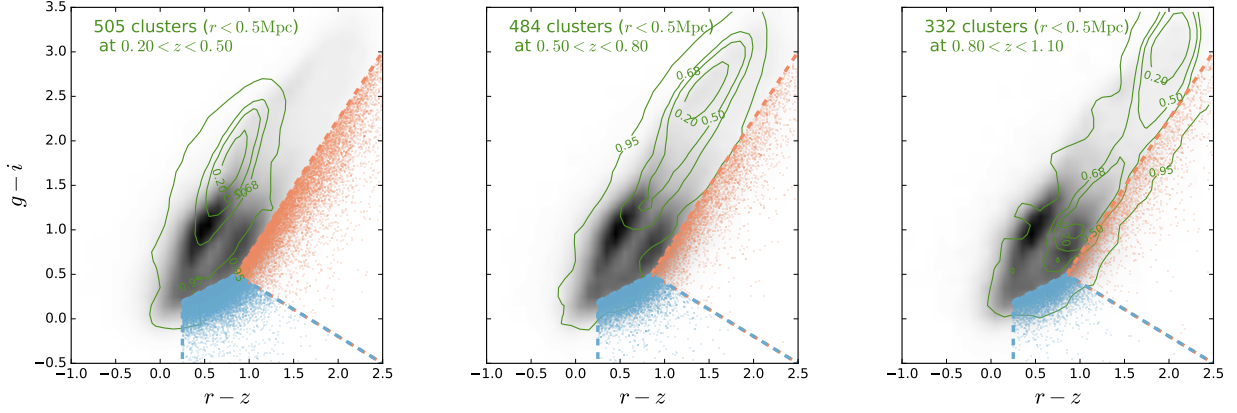


**Figure 2.** The color-color diagrams in  $g-i$  vs  $r-z$  showing (1) the selected low- $z$  and high- $z$  background populations in red and blue, respectively, (2) the distribution of the cluster galaxies as the green contours, and (3) the smoothed distribution of galaxies in the random fields as the underlying grey image. The cluster galaxies that lie projected within the clustercentric radius of 0.5 Mpc around the BCGs are used to derive the distribution of cluster galaxies (green contours), after the statistical background subtraction using the random fields. The random fields are randomly drawn from the HSC FDDFC footprint. The labels in the green contours represent the enclosed percentage of the selected cluster galaxies. The color-color selections for the low- $z$  and high- $z$  backgrounds are shown by the red and blue dashed lines, respectively. The left to right panels show the results of lower, medium, and higher redshift bins, respectively. These plots are produced by stacking the galaxies with  $i$ -band magnitude between 22 mag and 24.5 mag in the cluster fields and the same amounts of the randomly drawn apertures, for which the redshift range and the number of the pointing are labelled in the upper-left corner in each panel. We find clear concentration of cluster galaxies—which is the cluster red sequence—moving toward the upper-right corner in the color-color diagrams as increasing cluster redshift. On the other hand, a clear enhancement of galaxy concentration starts to appear at the colors of  $g-i \approx 1$  and  $r-z \approx 1$  for the high-redshift clusters at  $z \gtrsim 0.8$ , as an indication of increasing blue members in clusters.

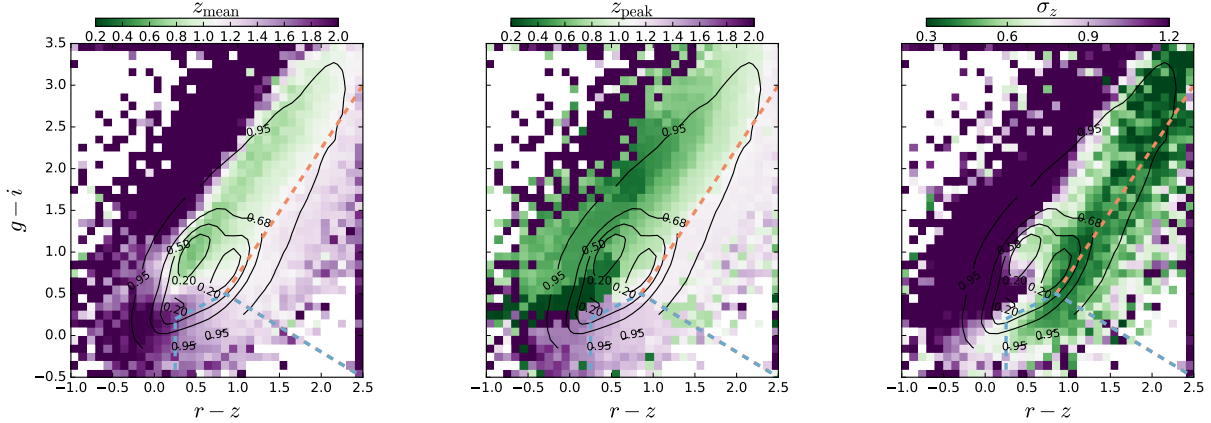


**Figure 3.** The color-color,  $g-i$  vs  $r-z$ , diagrams showing the mean  $z_{\text{mean}}$  (left), peak  $z_{\text{peak}}$  (middle), and the scatter  $\sigma_z$  (right) of the stacked  $P(z)$  of each color-color cell. These color-color cells are defined as the boxes with a width of 0.1 mag. The black contours in each panel represent the normalized distribution in the random fields, for which the labels show the enclosed percentage of the selected galaxies. These plots are produced by stacking the  $P(z)$  of the galaxies with  $i$ -band magnitude between 22 mag and 24.5 mag in the randomly drawn apertures. The color-color selections for the low- $z$  and high- $z$  backgrounds are, respectively, shown by the red and blue dashed lines. In this way, we can avoid the redshift-confusion regions (see the text).

cluster field. In this way, we can obtain the distribution of the cluster galaxies in the space of  $g-i$  vs  $r-z$  by statistically removing the fore/background. We only use the CAMIRA clusters with richness of  $N > 20$  and the galaxies with magnitude between 22 and 24.5 for the procedure above. We repeat this exercise for three redshift bins ( $0.2 < z \leq 0.5$ ,  $0.5 < z \leq 0.8$ , and  $0.8 < z \leq 1.1$ ). The results of three redshift bins are shown in Figure 2: The green contours are the distributions of the cluster galaxies after the statistical fore/background subtraction, and the underlying greyscale images represent the smoothed galaxy densities drawn from the random fields.

As the cluster redshift increases from the left to right panel in

Figure 2, it is clear that the cluster red sequence is moving toward the redder regime in both colors and that an increasing population of the cluster blue members appears at  $r-z \approx 0.9$  and  $g-i \approx 1$ . Our goal is to define the color-color cuts to avoid these two regions. Meanwhile, we want to select the background galaxy population with high purity and high number density. To do so, we further follow the guidance (ii) by making use of the photometric redshift. Specifically, we stack the probability distribution functions  $P(z)$  of the photometric redshift of all galaxies that lie within each color-color cell, and calculate the mean, peak and the scatter of the stacked  $P(z)$ . These color-color cells are defined as boxes with a width of 0.1 mag in the space of  $g-i$  vs  $r-z$ . This procedure is

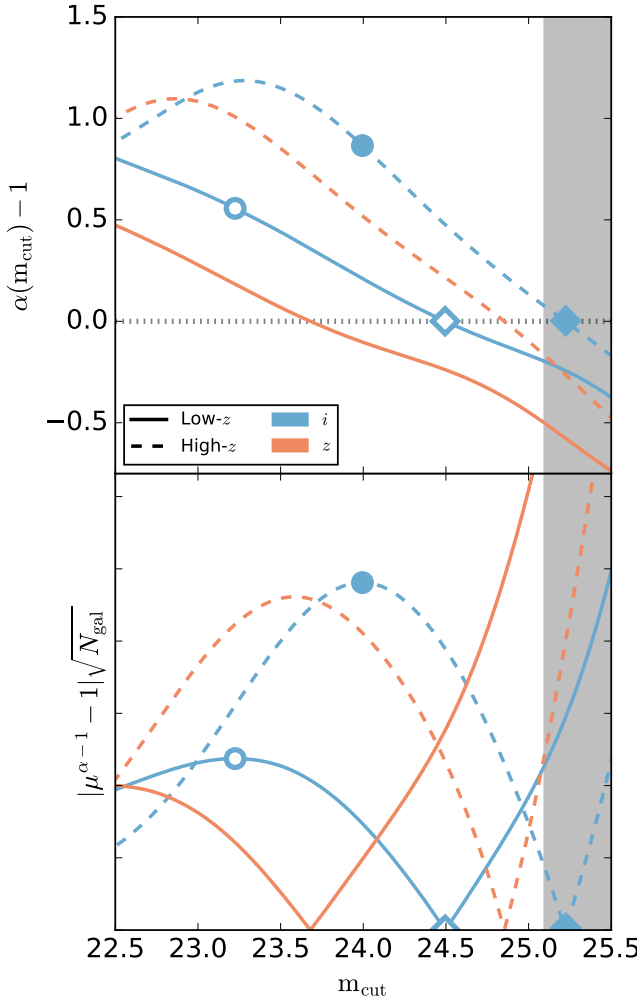


**Figure 4.** The expected signals (upper panel) and the signal-to-noise ratios (lower panel) of the magnification bias as a function of magnitude. The estimations of the low- $z$  and high- $z$  backgrounds are indicated by the solid and dashed lines, respectively. We show the results of the  $i$ -band in blue, while we also additionally present the results of the  $z$ -band in red, as a comparison. The dotted grey lines show the case of  $\alpha - 1 = 0$ , where the net magnification bias vanishes. The open (solid) circle and diamonds are the  $m_{\text{cut}}$  used for selecting the flux-limited “lensing-cut” and “null-test” samples, respectively, for the low- $z$  (high- $z$ ) background. The grey area presents the regime where the depth of  $i$ -band is below the  $10\sigma$  limiting magnitude.

performed on the random fields to avoid the clusters, for which the galaxy population has a biased distribution in the color-color space.

We use the  $P(z)$  estimated by DemP (Hsieh & Yee 2014), a machine-learning based code that has been extended to robustly obtain various properties of galaxies, including the redshift and stellar mass (Lin et al. 2017). The  $P(z)$  estimated by DemP are very well calibrated (Tanaka et al. 2018), suggesting no signs of bias according to the tests of the probability integral transform (PIT) and the continuous ranked probability score (Polsterer et al. 2016). In addition, the point estimates of the photometric redshift are accurate to better than 1% in term of  $\langle \Delta z / (1+z) \rangle$  with scatter of  $\approx 0.04$  and an outlier rate of  $\approx 8\%$  for galaxies with  $i < 24$  mag (Tanaka et al. 2018). More details of the calibration of photometric redshift can be found in Tanaka et al. (2018).

In Figure 3, we show the mean (left), peak (middle) and scat-

ter (right) of the stacked  $P(z)$  in the space of  $g-i$  vs  $r-z$ . The black contours in Figure 3 represent the normalized galaxy density with the labels showing the percentages of the enclosed galaxies. By comparing the left and middle panels in Figure 3, it is clear that there is severe degeneracy of the photometric redshift estimation between the redshift of  $\approx 0.5$  and  $\approx 2$  at the colors of  $g-i \approx 0.7$  and  $r-z \approx 0$ . This is also reflected in the right panel that the scatter of the stacked  $P(z)$  is significantly larger in the whole upper-left region. This suggests that either the true redshift distributions are wide in these color-color cells, or the photometric redshift is ill-constrained in these regions. On the other hand, the ideal background populations of the galaxies can be identified at the lower-right corner of the color-color space with mean redshift of  $1.1 \lesssim z \lesssim 1.6$  and small dispersion, avoiding the redshift-confusion regions.

Based on the guidance (i) and (ii) as well as the information of the galaxy number density in the color-color space, we select two background populations, as referred to the low- $z$  and high- $z$  backgrounds, respectively. The low- $z$  and high- $z$  backgrounds are shown by the red and blue points in Figure 2, respectively. In Figure 2 and Figure 3, we also mark the color-color selections by the dashed lines. These color-color cuts are defined such that we can minimize the regions overlapping with the clusters, while maximizing the source density with low dispersion in the stacked  $P(z)$ .

Although these color-color selections are optimized to select the sources with high purity, the selected populations are still likely to be contaminated by the cluster members, due to the fact that the color-color distribution of the cluster field is highly biased with respect to the random field. We will quantify this cluster contamination in Section 5.2, and correct for them in Section 5.6.

After the color-color selection, we need to further apply a magnitude cut because we measure the magnification bias using a flux-limited sample. As seen in equation (4), the signal of magnification bias is a function of the logarithmic count slope  $\alpha$ , which generally depends on the magnitude and the choice of the passband. The count slope  $\alpha$  is larger than 1 at bright end and is monotonically decreasing as increasing magnitude, thus we expect a density enhancement (depletion) for a cut at bright (faint) end. To anticipate a high signal of density enhancement, the slope  $\alpha$  is required to be much higher than 1, which is typically at very bright end where the Poisson noise is large. Conversely, a fainter magnitude cut results in a source sample with a larger size, thus the Poisson noise decreases. However, the signal is expected to become lower because of a smaller  $\alpha$  at the faint end. Therefore, one needs to optimize the magnitude cut ( $m_{\text{cut}}$ ) at the appropriate passband to achieve the highest signal-to-noise ratio. Motivated by this, we show the slopes and the relative signal-to-noise ratios as functions of magnitude in the passbands in the upper and lower panels of Figure 4, respectively. We note that we only show  $i$ - and  $z$ -band in Figure 4 for simplicity.

To anticipate the relative signal-to-noise ratios of magnification bias (as shown in the lower panel of Figure 4), we simply consider the Poisson noise as the only source of uncertainty. Based on equation (5), the signal-to-noise ratio of magnification bias is proportional to  $(\mu^{\alpha-1} - 1) / (\sqrt{N_{\text{Ngal}}}/N_{\text{Ngal}}) = (\mu^{\alpha-1} - 1) \sqrt{N_{\text{Ngal}}}$  for a given cluster, where  $N_{\text{Ngal}}$  is the total counts of the background sources of interested. Then, we estimate  $N_{\text{Ngal}}$  of the low- $z$  and high- $z$  backgrounds using all the sources located in the FDFC footprint to produce the lower panel of Figure 4. The results of the low- $z$  and high- $z$  populations are the solid and dashed lines, respectively.

Although slightly higher signal-to-noise ratios are expected

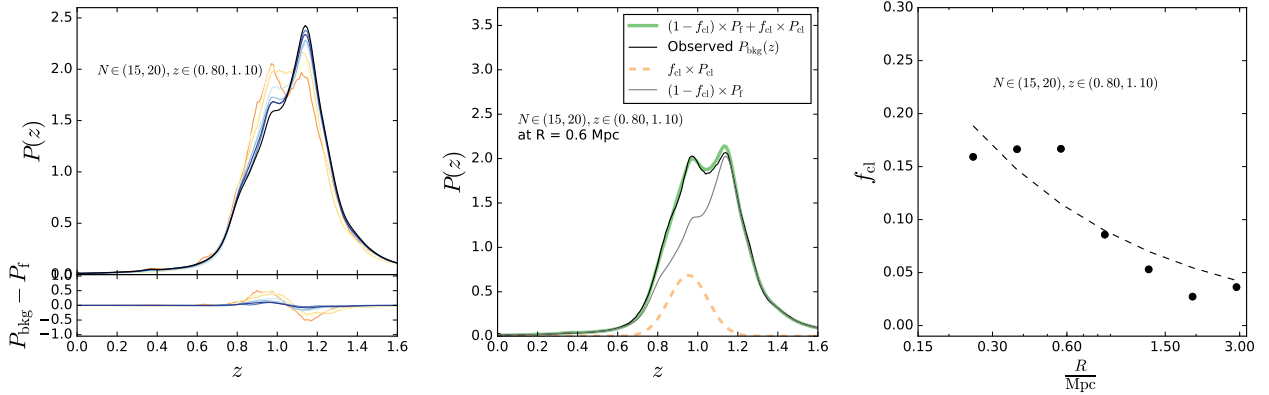


**Figure 5.** The plots demonstrating the  $P(z)$ -decomposition method (Gruen et al. 2014) in estimating the cluster contamination. We show the results of the low- $z$  background for the clusters with richness of  $15 \leq N < 20$  at redshift  $0.8 \leq z < 1.1$ , as an example (see Section 5.2). The upper subplot of the left panel shows the stacked probability redshift distributions  $P(z)$  of the selected source sample, with redder color as decreasing clustercentric radius; the one from the random fields is shown in black. To highlight the cluster contamination in terms of  $P(z)$ , we also show the difference between the observed clusters  $P_{\text{bkg}}(z)$  and the random fields  $P_t(z)$  in the lower subplot of the left panel. The enhancement of probability in the cluster redshift range  $0.8 \leq z < 1.1$  is clearly seen in the cores of clusters. The middle panel demonstrates the  $P(z)$ -decomposition method in the radial bin of  $R \approx 0.6$  Mpc: the observed redshift distribution  $P_{\text{bkg}}$  is in black; the redshift distributions of the random fields  $P_t$  and the clusters  $P_{\text{cl}}$  normalized by the  $(1 - f_{\text{cl}})$  and  $f_{\text{cl}}$  are in grey and yellow lines, respectively; the best-fit redshift distribution is shown by the green line. The right panel shows the results of the derived cluster contamination profile  $f_{\text{cl}}(R)$  with the best-fit power law indicated by the dashed line.

for bluer bands (e.g., the  $g$ - and  $r$ - bands), we stress that we do not use them to select the flux-limited sample for the analysis of magnification bias. This is because the variation of seeing in both  $g$ - and  $r$ - bands is large ( $\approx 0.5'' - 1.3''$ ), which introduces significant non-uniformity across the field. On the other hand, the HSC observing strategy specifically requires the  $i$ -band imaging to be taken under a good seeing condition, resulting in a much more uniform seeing distribution across the field (Mandelbaum et al. 2018). In this regard, we only use  $i$ -band for the analysis of magnification bias in this work. We apply a magnitude cut of  $m < m_{\text{cut}}$  in the  $i$ -band after the color-color selection to construct the flux-limited sample, such that the maximized signal-to-noise ratio of the magnification bias measurement is expected. Specifically, we use  $m_{\text{cut}} = 23.2$  mag and  $m_{\text{cut}} = 24$  mag for the low- $z$  and high- $z$  populations, which are marked by the solid and open circles in Figure 4, respectively. We refer to these samples as the “lensing-cut” samples.

On the other hand, there exists a special magnitude where  $\alpha = 1$ , such that we do not expect the magnification bias signal with the magnitude cut of  $m < m_{\text{cut}}$  (see Section 2). With this sample, we can verify our magnification bias measurements of the “lensing-cut” sample, and quantify the residual biases, if any. For the low- $z$  (high- $z$ ) background, this limiting magnitude is  $m_{\text{cut}} = 24.5$  mag ( $m_{\text{cut}} = 25.2$  mag), which is marked by the open (solid) diamond in Figure 4. Therefore, we independently construct the flux-limited samples with these magnitude cuts for both low- $z$  and high- $z$  backgrounds, for which we refer to as the “null-test” samples. We will use the “null-test” samples to validate our magnification bias measurements (see Section 5.4).

For both “lensing-cut” and “null-test” samples, we all further discard the galaxies with  $i < 22$  mag to minimize the contamination of non-background galaxies. The resulting number densities are 0.44 and 0.90 galaxies per square arcmin for the low- $z$  and high- $z$  populations, respectively. The mean redshift of the low- $z$  and high- $z$  populations are  $\approx 1.1$  and  $\approx 1.4$ , respectively.

In this work, we focus on the density enhancement of magnification bias at relatively bright end with  $\alpha - 1 \gg 0$ . It is worth mentioning that we cannot probe the density depletion of magnification

bias in the regime of  $\alpha \ll 1$ , where the detection is significantly suffering from the shot noise at very faint end ( $i \gtrsim 25.5$  mag). The grey area in Figure 4 shows the magnitude fainter than 25.1 mag, which is the  $10\sigma$  depth of the  $i$ -band, indicating that the source detection starts to be dominated by the shot noise.

## 5.2 Cluster Member Contamination

One of the most critical bias in cluster lensing using a photometry-selected source sample is the cluster contamination. That is, cluster members could leak into the source sample, causing bias in lensing signals. For example, the average tangential shear of the selected background sample is diluted by the cluster contamination, thus resulting in a biased-low mass estimate. In the case of magnification bias, the leaked cluster members result in a density enhancement that is not due to gravitational lensing but the clustering of member galaxies, returning a biased high (low) magnification-inferred mass for the case of  $\alpha > 1$  ( $\alpha < 1$ ). Moreover, the cluster contamination is expected to vary with the clustercentric radius, cluster redshift and the cluster mass. In this regard, this is necessary to quantify and account for the cluster contamination, if any.

In this work, the cluster contamination is quantified by the method developed in Gruen et al. (2014), which has been widely used in other cluster lensing studies (Chiu et al. 2016a; Melchior et al. 2017; Dietrich et al. 2019; Medezinski et al. 2018; McClintock et al. 2019). This demonstrates a robust approach to successfully estimate and correct for the cluster contamination (Varga et al. 2018). In what follows, we briefly summarize this method and refer the reader to Gruen et al. (2014) for more details.

The basic idea of this method is to decompose the photometric redshift distribution,  $P_{\text{bkg}}(R, z)$ , of the selected background sample observed at the clustercentric radius of  $R$  into two components, the photometric redshift distributions of the source sample  $P_t(z)$  and the cluster members  $P_{\text{cl}}(z)$ , using a linear relation of

$$P_{\text{bkg}}(R, z) = (1 - f_{\text{cl}}(R))P_t(z) + f_{\text{cl}}(R)P_{\text{cl}}(z), \quad (6)$$

where  $f_{\text{cl}}(R)$  is the cluster contamination at the radius  $R$ , and

$0 \leq f_{\text{cl}}(R) \leq 1$ , by definition. Here,  $P_{\text{f}}(z)$  is estimated by the source galaxies selected in the apertures randomly drawn from the field, and  $P_{\text{cl}}(z)$  is characterized by a normal distribution with the mean  $\mathbb{Z}_{\text{cl}}$  and standard deviation  $\sigma_{\text{cl}}$  that need to be constrained. In this way, the cluster contamination  $f_{\text{cl}}(R)$  can be derived for the observed  $P_{\text{bkg}}(R, z)$  at the projected radius  $R$ .

In practice, we have to stack the clusters to obtain the meaningful constraints of  $f_{\text{cl}}$ , because the the observed photometric redshift distribution is too noisy to carry out this method on a basis of individual clusters. Specifically, we stack clusters into three redshift bins ( $0.2 \leq z < 0.5$ ,  $0.5 \leq z < 0.8$ ,  $0.8 \leq z < 1.1$ ) and three richness bins ( $15 \leq N < 20$ ,  $20 \leq N < 30$ ,  $30 \leq N$ ), with nine bins in total. Again, we use the probability distribution functions of the photometric redshift estimated by DemP to estimate the cluster contamination.

For a radial bin in each richness and redshift bin, there are three parameters ( $f_{\text{cl}}$ ,  $\mathbb{Z}_{\text{cl}}$ ,  $\sigma_{\text{cl}}$ ) to be fitted. Similarly to Melchior et al. (2017), we jointly fit the mean  $\mathbb{Z}_{\text{cl}}$  and standard deviation  $\sigma_{\text{cl}}$  of the normal distribution (representing  $P_{\text{cl}}(z)$  in equation (6)) for the same redshift bin, while the cluster contamination  $f_{\text{cl}}$  is varying in each richness and radial bin. The result of the binning of  $15 \leq N < 20$  at  $0.8 \leq z < 1.1$  is shown in Figure 5, as the example of highly contaminated regimes. In the left panel, we show the  $P_{\text{bkg}}(z)$  of the low- $z$  background at different clustercentric radii (the red-der, the inner). There is an increasing enhancement in the stacked  $P_{\text{bkg}}(z)$  at the cluster redshift range of  $0.8 \lesssim z \lesssim 1.1$  as decreasing clustercentric radius, clearly indicating the cluster contamination. In the middle panel, the decomposition of  $P_{\text{bkg}}(z)$  at the radius of  $r \approx 0.6$  Mpc is shown. Moreover, this cluster contamination can be well modelled by a normal distribution (the yellow dashed line).

Motivated by Applegate et al. (2014), we further fit a power-law profile in radius normalized at 1 Mpc,

$$f_{\text{cl}}(R) = f_{\text{cl}, 1\text{Mpc}} \times \left( \frac{R}{1 \text{ Mpc}} \right)^{\alpha_{\text{cl}}},$$

to the derived  $f_{\text{cl}}$  profile to statistically account for the cluster contamination as a function of radius. The fitting of the normalization and power-law index ( $f_{\text{cl}, 1\text{Mpc}}$ ,  $\alpha_{\text{cl}}$ ) is performed for every richness and redshift bins, which is sufficient to describe the radial trend of  $f_{\text{cl}}$ , as shown by the dashed line in the right panel of Figure 5. We have tried the fitting with varying  $\mathbb{Z}_{\text{cl}}$  and  $\sigma_{\text{cl}}$  in each bin (instead of jointly fitting), which returns a consistent result.

There are some caveats of the cluster contamination estimated by the Gruen et al. (2014) method, in which the fundamental assumption is that the observed  $P(z)$  of the selected background population in the cluster fields is statistically identical to that observed in the random fields. This assumption might be broken due to the degraded performance of photometry in crowded fields, such as clusters. The assessment using the hscPipe around the cluster fields (see Section 5.3) quantifies that less than 5% of the sources are heavily blended with the member galaxies or even missed in the cluster fields. This suggests that photometry for majority of the source galaxies is not significantly affected by the cluster members. The photometry performance of the hscPipe around the cluster fields will be further investigated in the forthcoming paper (Murata in prep.).

Another concern regarding cluster fields is the presence of Intra-Cluster Light (ICL), which could bias the photometry, photo- $z$ , and/or mass modelling. Gruen et al. (2018) estimate the impact of the ICL on the mass modelling, suggesting a bias of  $\lesssim 2\%$  in the differential surface mass profile at  $r \gtrsim 300$  kpc for clusters with  $M_{500} \lesssim 3 \times 10^{14} M_{\odot}$ . This amount is negligible compared to the

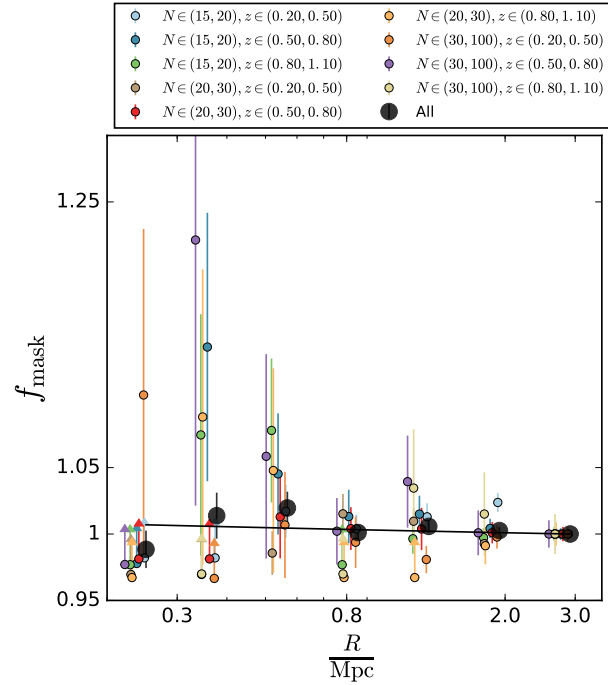


**Figure 6.** The corrections for the masking effect in the high- $z$  background populations by using the synthesis galaxies generated by the Synpipe code. The resulting  $f_{\text{mask}}$  in different richness and redshift bins is color-coded, as shown in the figure. The black points are the masking correction estimated by stacking all clusters. The black curve is the best-fit power law, which is ultimately used to statistically correct for the masking effect. We note that we normalize the masking correction to the outer most bin  $R_{\text{out}}$  (see the text in Section 5.3), such that  $f_{\text{mask}}(R_{\text{out}}) = 1$  to remove the effect of random masking. In some cases that we do not have masked synthesis galaxies in the radial bins, we mark the data points as the lower bounds shown by the arrows.

current statistical uncertainty in this work, therefore we ignore this effect.

To validate the derived cluster contamination, one typically needs a very detailed and customized simulation (Varga et al. 2018) or the spectroscopic observations of the cluster field to further identify the cluster members, which are not currently available to our sample. However, we can in principle empirically validate the magnification measurements of the “lensing-cut” sample based on the “null-test” sample (see Section 5.1), if there exists any residual bias caused by the inaccurate correction for the cluster contamination. We will return to this in Section 5.4.

### 5.3 Masking Correction

Another complexity that could bias the observed magnification bias around clusters is the masking effect: Bright member galaxies could mask the sources behind clusters, effectively mimicking the density depletion as the decreasing clustercentric radius. This bias can be approximated by calculating the fractional angular area occupied by the bright member galaxies in each radial bin, as described in Umetsu et al. (2011). Another approach is to run realistic image simulations of cluster fields to access the successful rate of the source detection as a function of clustercentric radius, as demonstrated in Chiu et al. (2016a). Nevertheless, simulating the realistic galaxy population in clusters requires the prior knowledge



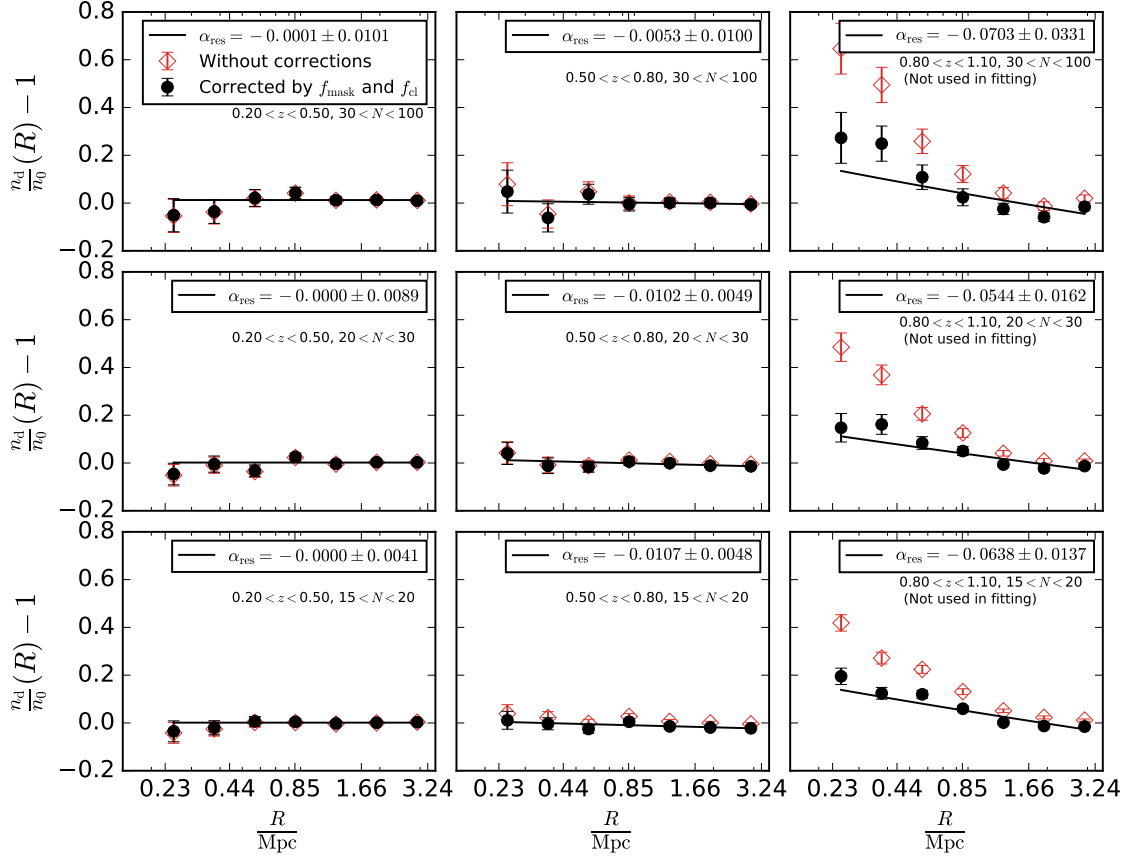


**Figure 7.** The stacked density contrast of the “null-test” sample (see Section 5.1) for the low- $z$  background as functions of clustercentric radius in three richness (lower to upper) and three redshift (left to right) bins. The red diamonds are the direct measurements of  $\omega(R)$  without any correction, while the black circles are measurements after the corrections for the cluster contamination  $f_{cl}$  and masking  $f_{mask}$ . The deviation of  $\frac{n_d}{n_0} - 1$  from zero indicates the residual bias. The best-fit power-law models (equation (9)) are indicated by the black curves with the best-fit radial indices  $\alpha_{res}$  shown in the upper-right corners. As seen in this plot, we observe significant residual bias in the highest redshift bin ( $0.8 < z < 1.1$ ), for which we ignore this redshift range in our analysis. These estimations of residual bias are used to quantify the systematic uncertainty of our final results.

of cluster mass and the  $N$ - $M$  relation, for which this approach is circular and thus not ideal for this work.

In this work, we improve the method in Chiu et al. (2016a) by directly simulating galaxies of interest in the real imaging. This method is similar to Suchyta et al. (2016) and Chiu et al. (2016), where they embedded synthesis galaxies to the real imaging to quantify various observational systematics. Specifically, we embed synthesis galaxies in the observed images, processed by the identical pipeline, to access the source detection around the cluster field. This is done by using the Synpipe (Huang et al. 2018), a Python package which embeds synthesis galaxies and runs the end-to-end hscpipe pipeline to validate the performance of the photometric measurements. The brief summary of Synpipe is given below, and we refer the reader to Huang et al. (2018) and Murata in prep. for more details.

The real galaxies in the COSMOS field (Capak et al. 2007; Ilbert et al. 2009), which are modelled by a single-Sersic galaxy template (Lackner & Gunn 2012) based on the observed *HST*/ACS images, are used as the input of the synthetic galaxies. The input catalog of the synthesis galaxies is flux-limited with  $I_{F814} \leq 25.2$  mag, which is also implemented in the simulation toolkit Galsim (Rowe

et al. 2015). The injection of the synthesis galaxies is carried out on a basis of single-epoch images, convolved with the locally measured PSF, followed by the realistic Poisson noise added. The synthesis galaxies are embedded in grids with a separation of  $15''$  to avoid the self-blending. Nine identical inputs are used for every  $3 \times 3$  grid. Due to the extremely large demand for computation, Synpipe is only run on the *i*-band imaging in the GAMA09h field, corresponding  $\approx 43 \text{ deg}^2$ . After re-detecting the embedded synthesis galaxies, the resulting catalog is matched to the HSC-Wide-depth COSMOS catalog, which is also observed by the HSC survey, via their unique IDs to obtain the five-band HSC photometry. That is, the final Synpipe catalog contains not only the realistic colors from the HSC survey itself, but also the information of source detection that is subject to the galaxy type and the local properties of the footprint. Because the real galaxies observed in the COSMOS field are used for the input synthesis catalog of Synpipe, we stress that the embedded galaxies naturally capture the underlying correlation between the galaxy properties (e.g., the morphology) and the magnitude.

Next, we apply the same background selections (as in Section 5.1) to the resulting Synpipe catalog. Then, we stack the

galaxy number profiles around the CAMIRA clusters to derive the detection rate of the embedded source galaxies. In this way, the masking correction at the clustercentric radius  $R$  is defined as

$$f_{\text{mask}}(R) = \frac{1}{1 - \frac{N_{\text{syn,mask}}(R)}{N_{\text{syn,tot}}(R)}} = \frac{N_{\text{syn,tot}}(R)}{N_{\text{syn,tot}}(R) - N_{\text{syn,mask}}(R)}, \quad (7)$$

where  $N_{\text{syn,mask}}(R)$  and  $N_{\text{syn,tot}}(R)$  are the numbers of synthesis galaxies (after the background selection) at the projected radius  $R$  that are masked and embedded, respectively. To derive a more precise masking correction, we need to stack clusters. In the stacking procedure, we evaluate  $N_{\text{syn,tot}}(R)$  and  $N_{\text{syn,mask}}(R)$  by summing the synthesis galaxies at the clustercentric radius  $R$  around all clusters in the bin of interest, i.e.,

$$N_{\text{syn,mask}}(R) = \sum_{i\text{-th cluster} \in \text{bin}} N_{\text{syn,mask}_i}(R),$$

and

$$N_{\text{syn,tot}}(R) = \sum_{i\text{-th cluster} \in \text{bin}} N_{\text{syn,tot}_i}(R).$$

We note that the  $f_{\text{mask}}(R)$  correction is then normalized to one at the outermost radial bin  $R_{\text{out}}$ , i.e.,  $f_{\text{mask}}(R) \rightarrow f_{\text{mask}}(R)/f_{\text{mask}}(R_{\text{out}})$ , because we do expect that the source detection suffers from random masking even without clusters. That is, we only consider the radial trend of the masking effect raised from clusters, effectively removing the effect of random masking by re-normalization. For the low- $z$  and high- $z$  background populations, the random masking is  $\approx 2\%$ .

There are 491 CAMIRA clusters with  $N \geq 15$  at  $0.2 \leq z < 1.1$  in the GAMA09h field that is contained in the resulting Synpipe catalog. We divide the sample as stated in Section 5.2, to investigate the possible dependence of  $f_{\text{mask}}$  on the cluster richness or redshift. The result of the low- $z$  and high- $z$  backgrounds are similar, therefore we only show the latter in Figure 6, as a demonstration. In the case of  $N_{\text{syn,mask}}(R) = 0$  at some small radii, we mark the data point as the lower bound in Figure 6. By stacking all clusters, the masking correction  $f_{\text{mask}}$  (the black points) shows a near zero radial trend, with  $\approx 1.5\%$  in the cluster cores ( $r \lesssim 0.3$  Mpc). In addition, there is no strong indication for the dependence on richness or redshift, although the uncertainties remain large. Thus, we derive the final masking correction based on the  $f_{\text{mask}}$  of stacking all clusters (the black points). We note that we re-calculate  $N_{\text{syn,mask}}(R)$  and  $N_{\text{syn,tot}}(R)$  in equation (7) for each binning in Figure 6, instead of directly stacking the values of  $f_{\text{mask}}(R)$  to obtain the black points. The final masking correction is obtained by fitting equation (8) to the  $f_{\text{mask}}$  of stacking all clusters regardless of the richness and redshift.

$$f_{\text{mask}}(R) = f_{\text{mk},1\text{Mpc}} \times \left( \frac{R}{0.1 \text{ Mpc}} \right)^{\alpha_{\text{mk}}}. \quad (8)$$

The best-fit model for  $f_{\text{mask}}$  is shown by the black curve in Figure 6. We note that this correction is in agreement with the one estimated in Tudorica et al. (2017), for which the masking correction for the  $u$ -dropout sources is  $\approx 1.05$  at  $r \approx 0.3$  Mpc monotonically decreasing to  $\lesssim 1.035$  at large radii ( $r \gtrsim 3$  Mpc), with an increase of  $\lesssim 2\%$  toward the cluster cores.

We note that there are two assumptions implicitly made in this approach: (1) The masking effect of the clusters estimated in the GAMA09h field is the same as the other fields, statistically. This is a reasonable assumption, given that the seeing distribution of the GAMA09h field is a good representative for the other fields (Mandelbaum et al. 2018). (2) Once the sources are successfully detected

by hscPipe, we assume that their photometry performance is not significantly degraded because of the masking effect. That is, to first order we only consider the masking effect on the detectability of the sources, and assume that the pipeline can successfully deblend the fluxes coming from the neighboring objects as long as the sources are detected. Therefore, we can directly obtain the photometry (colors and magnitude, specifically) relying on the external catalog of the HSC-Wide-depth COSMOS field, where no masking effect due to massive clusters exists. However, the masking indeed could affect the photometry in practice. Moreover, this might be a chromatic effect, which possibly depends on the galaxy type of cluster members and, therefore, the cluster mass and redshift as well. To access this, a detailed run of Synpipe on the whole HSC survey with the synthesis galaxies embedded in the five bands is clearly warranted. In this work, we choose to empirically validate our magnification bias signals based on the “null-test” sample (see Section 5.4 for more details), if any residual bias of the masking effect persists.

#### 5.4 Validating the Measurements of Magnification Bias

Our goal is to obtain the unbiased measurements of magnification bias and use it to constrain the underlying  $N$ – $M$  scaling relation. To achieve this, we have statistically corrected for the known biases, such as the cluster contamination existing in the photometrically selected source samples (see Section 5.2) and the masking effect due to the cluster member galaxies (see Section 5.3). However, these corrections could be insufficient due to the over-simplified assumptions, as follows.

For example, we assume that the performance of the photometric redshift estimates in the crowded fields of clusters is statistically the same as the random fields, such that we can exploit the method of  $P(z)$ -decomposition to extract the cluster contamination. If the photometric redshift distribution is different in the cluster fields, then the extracted cluster contamination would be inevitably biased. Another caveat is that we assume that the photometry in the cluster fields are not severely degraded. Therefore, we can investigate the masking effect based on the photometry obtained from the external COSMOS catalog. Relating to the photometry in the crowded fields, it is also known that the current hscpipe tends to over-deblend the bright objects (Huang et al. 2018), which could result in an artificial enhancement in the number density around bright cluster members.

Among of the concerns above, the most important one is probably the (deblended) photometry in the cluster fields, for which the bias in photometry could be propagated to the photo- $z$  estimation and the analysis afterward. The photometry of the selected sources could be biased due to imperfect deblending: If the flux of cluster members leaks into the neighboring source at the background, then this would result in a biased-high flux of the source and, therefore, a biased-high number density of the source sample above the flux threshold. This would mimic the density enhancement of magnification bias. Vice versa, if the flux of the background source is lost due to a failure in deblending, then the number density of the flux-limited sample would be biased-low, introducing the density depletion that is not due to gravitational lensing. In addition, this bias is expect to depend on the clustercentric radius. On the other hand, the blending effect could exist in multi-wavelength, resulting in biased color that could further sabotage the color-color source selection. To this end, the blending effect could also depend on the broadband filters and the galaxy types, as well as the relative sizes and brightness of the blended sources and cluster members.

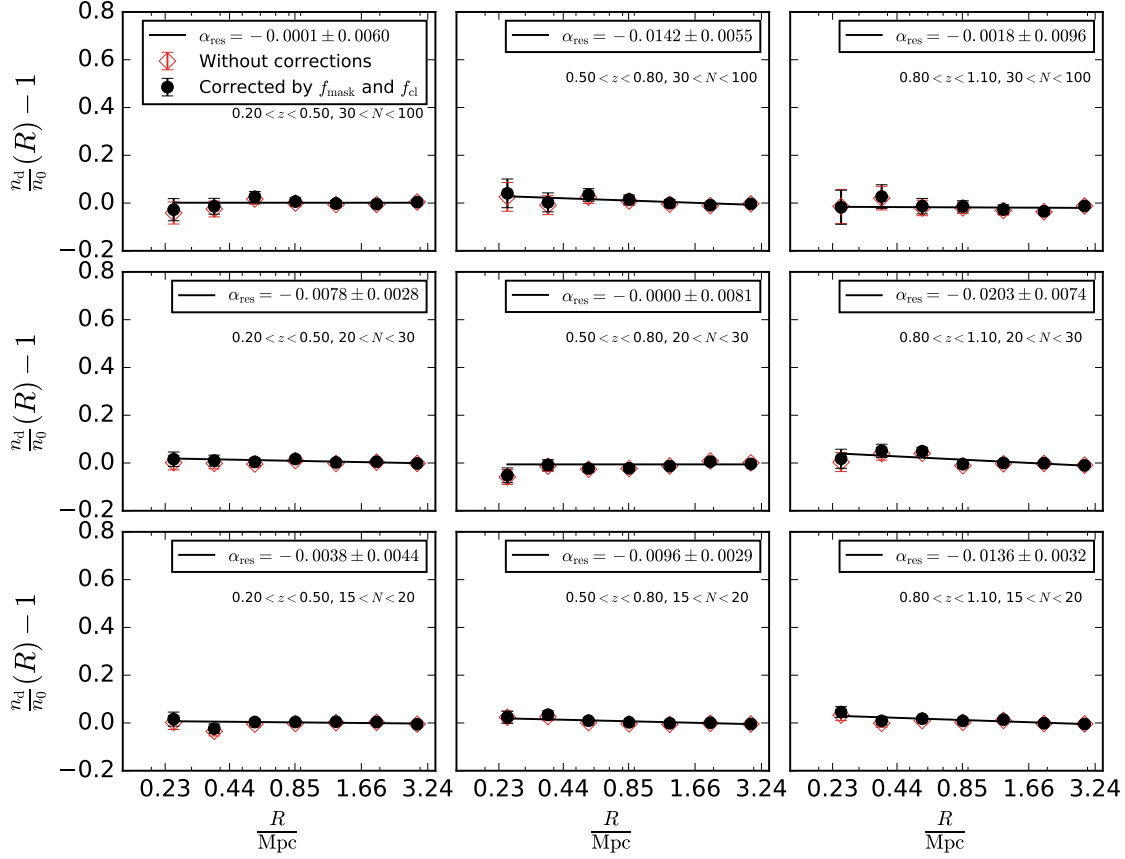


**Figure 8.** The validation of the magnification measurements for the high- $z$  background. This plot is produced in the same way as in Figure 7. We do not observe significant residual bias in the case of using high- $z$  background, therefore all redshift and richness bins of magnification bias are used in fitting the scaling relation.

This implies that the masking effect might correlate with the cluster mass and redshift. In a nutshell, the crowded field is expected to have impact on the source selection, photometry and therefore the performance of the photometry redshift estimation in a very subtle but complex way, which is very hard to quantify without a realistic and end-to-end simulations. A detailed investigation is clearly warranted (Murata in prep.).

In this work, we choose to empirically validate for the magnification measurements. Specifically, we carry out the same end-to-end analysis on the “null-test” sample, for which the net magnification effect vanishes because of  $\alpha - 1 = 0$  (see Section 2 for more details). We use the “null-test” sample to empirically access the residual bias that could exist in the measurements of the “lensing-cut” sample. The only assumption made in this approach is that we assume the residual bias is the same between these two samples. This is a reasonable assumption, to the first order, given that the “null-test” sample is selected as the population with the same color as the “lensing-cut” sample, except generally  $\approx 1$  mag deeper. To be exact, the “null-test” sample is  $\approx 1.3$  mag and  $\approx 1.2$  mag deeper than the “lensing-cut” sample for the low- $z$  and high- $z$  background populations, respectively. As a fact, we also do not observe any significant difference in the derived cluster contamination  $f_{cl}$  and masking correction  $f_{mask}$  between the “null-test” and “lensing-cut”

samples. This suggests that the residual bias, if exist, is expected to be consistent between these two.

To extract the residual bias, we perform the identical analysis on the “null-test” samples to derive the profiles of the density contrast  $\frac{n_d}{n_0}(R)$ . We use the same binning scheme according to the cluster richness and redshift (as in Section 5.2 and Section 5.3), and then apply the corrections of  $f_{cl}$  and  $f_{mask}$  that are re-derived based on their  $m_{cut}$ . The results of the “null-test” sample of the low- $z$  background is demonstrated in Figure 7, where the red diamonds and black circles represent the profiles of  $\frac{n_d}{n_0}(R) - 1$  before and after the corrections (both  $f_{cl}$  and  $f_{mask}$ ), respectively. To be more quantitative, we fit the density contrast  $\frac{n_d}{n_0}(R)$  of each richness and redshift bin by a power-law relation,

$$f_{res}(R) = f_{res,1\text{Mpc}} \left( \frac{R}{1\text{Mpc}} \right)^{\alpha_{res}}, \quad (9)$$

where  $f_{res,1\text{Mpc}}$  is the normalization, and  $\alpha_{res}$  is the radial index (as shown in Figure 7).

In Figure 7, we clearly observe the biased-high density enhancement (the black circles) toward the cluster centers for the high-redshift clusters at  $0.8 \leq z < 1.1$ ; the derived  $\alpha_{res}$  are all deviating from zero with high significance. Moreover, the high-richness clusters with  $30 \leq N < 100$  show larger residual bias than the low-richness clusters ( $15 \leq N < 20$  and  $20 \leq N < 30$ ), especially in

the cluster cores. The fact that the severe residual bias exists in our magnification measurements of the “null-test” sample—even after the corrections for the cluster contamination and masking—for the clusters at high redshift ( $z \geq 0.8$ ) suggests a failure related to the photometry in the extremely crowded fields. On the other hand, there is no clear indication that the magnification measurements are significantly corrupted for other richness-redshift bins. This suggests that the low- $z$  background is a highly pure sample for studying the clusters at  $z < 0.8$ . Therefore, we choose not to use the magnification measurements from the low- $z$  background for the clusters at  $0.8 \leq z < 1.1$ .

The results of the high- $z$  background are shown in Figure 8. For the case of the high- $z$  background, we find that the density contrast  $\frac{n_d}{n_0}(R) - 1$  is all statistically consistent with zero for each richness and redshift bin. This suggests that we can obtain the magnification measurements free from the residual bias for the high- $z$  background. Therefore, the magnification measurements derived from the high- $z$  background are used for all clusters.

### 5.5 Magnification Bias Profiles

In this section, we extract the observable of magnification bias using the contrast of the number density profiles. In what follows, details are given.

For each cluster, we cross-correlate the position of the BCG, as the cluster center, with the source catalog by the estimator,

$$\omega(R) = \frac{\text{LS}(R)}{\text{LR}(R)} - 1, \quad (10)$$

where the symbols of LS( $R$ ) and LR( $R$ ) are the normalized numbers of the cluster-source and cluster-random pairs with the projected separation of  $R$ , respectively. We construct a large random catalog ( $\approx 100$  times larger than the source catalog) that has the same geometric layout as the HSC FDFC footprint accounting for the brightstar- and defect-mask (Coupin et al. 2018). Because we derive the estimator  $\omega$  for each cluster separately, we do not need to build the random catalog for the clusters. We use seven logarithmic radial bins ranging from 0.2 Mpc to 3.5 Mpc in the physical unit for each cluster, ensuring that we are probing the same portion of the radial profiles of the clusters at different redshifts. We have confirmed that discarding the inner most bin does not significantly affect the final results (see the last column of Table 1). Finally, the magnification bias profile  $\Delta_\mu$  is derived after statistically accounting for the cluster contamination (Section 5.2) and the masking effect (Section 5.3). Specifically,  $\Delta_\mu(R)$  at the radius  $R$  can be derived as follows.

$$\Delta_\mu(R) = (\omega(R) + 1) \times (1 - f_{\text{cl}}(R)) f_{\text{mask}}(R) - 1. \quad (11)$$

The correction for the cluster contamination (the masking effect) is  $f_{\text{cl}}$  ( $f_{\text{mask}}$ ) evaluated at the radius of  $R$  in the richness and redshift bin where the cluster locates. For each cluster, we repeat the whole procedure described above for the low- $z$  and high- $z$  backgrounds with both “lensing-cut” and “null-test” samples each (see Section 5.1 for the definitions of the “lensing-cut” and “null-test” selection).

We also carry out the same analysis on the random fields to access the possible bias in the estimator of  $\omega$ . Specifically, we randomly draw the same amount of apertures in the HSC FDFC footprint with the same physical sizes of each cluster in each richness-redshift bin, and repeat equation (11) without the corrections for the cluster contamination and the masking effect (i.e.,  $f_{\text{cl}}(R) = 0$  and  $f_{\text{mask}}(R) = 1$ ). If the estimator on the HSC fields is unbiased,

then we expect that  $\omega(R)$  is statistically consistent with zero. The results are shown as the grey area in Figure 11 and Figure 12 for the low- $z$  and high- $z$  backgrounds, respectively. Notwithstanding the measurements of the random fields are noisy, we observe a mildly systematic offset deviating from zero that persists out to large radii. If we stack all clusters together, the global offsets  $\delta$  are  $-0.0047 \pm 0.0028$  and  $-0.0070 \pm 0.0030$  for the low- $z$  and high- $z$  backgrounds, respectively. This offset reflects the imperfect star mask that is failed to capture the outer parts of bright stars at a sub-percent level. This results an over-sampled random catalog around the edges of bright stars and, therefore, a resulting biased-low  $\omega(R)$ . This needs to be accounted for, because this amount of offset is comparable to the signal of the 2-halo term, which is included in our modelling (see Section 5.6). It is important to note that this global offset is independent of clusters and has no radial dependence. Thus, we choose to marginalize this bias  $\delta$  in our forward-modelling approach (see Section 5.6).

The observed and corrected magnification profiles are still deviated from the underlying ones due to the presence of the measurement uncertainty, uncorrelated large-scale structure, and the intrinsic scatter at fixed mass. In this work, these factors above are characterized and accounted for by the covariance matrices that are directly derived from the data, following the same approach in Melchior et al. (2017). Specifically, we conduct a spatial jackknife technique that divides the footprint into 300 equal-area patches on the sky using a  $k$ -means algorithm<sup>1</sup>, followed by the same amount of repetition of deriving the measurements, i.e., equation (11), while omitting one patch each time. For the  $j$ -th repetition with  $j$ -th patch omitted, we concatenate the measurements as a data vector denoted by  $\Delta_{\mu(j)}$ . Then, the data covariance matrix is obtained as

$$\mathbb{C} = \frac{N_K - 1}{N_K - N_D - 2} \frac{N_K - 1}{N_K} \sum_{j=1}^{N_K} \left( \Delta_{\mu(j)} - \Delta_{\mu(\cdot)} \right)^T \cdot \left( \Delta_{\mu(j)} - \Delta_{\mu(\cdot)} \right), \quad (12)$$

where  $\Delta_{\mu(\cdot)} = \frac{1}{N_K} \sum_{j=1}^{N_K} \Delta_{\mu(j)}$ ,  $N_D$  is the total number of the measurements in the data vector, and  $N_K$  is the number of the equal-area patches, i.e.,  $N_K = 300$ . The inclusion of the first term,  $\frac{N_K - 1}{N_K - N_D - 2}$ , is needed because the noisy covariance matrix tends to underestimate the uncertainty (Hartlap et al. 2007). The size of one jackknife patch corresponds to the physical radius of  $\gtrsim 8$  Mpc for the cluster at  $z > 0.2$ , which is suitable for the radial scale of interest in this work. We have verified that the resulting covariance matrix is converged and is not sensitive to the current choice of  $N_K$ . The results of normalized covariance matrix (i.e., the correlation matrix) of the high- $z$  background is presented in Figure 9, as an example.

We do not observe significant cross-correlation of the magnification measurements among different richness and redshift bins, as demonstrated in the left panel of Figure 9, although the correlation matrices are noisy. Thus, we treat the magnification measurements of different richness-redshift bins as the independent measurements. We also derive the full covariance matrix by calculating equation (12) using all clusters without the richness and redshift binning. The full correlation matrix is shown in the right panel of Figure 9. We confirm that there is no significant difference in term of the radial correlation pattern between the subsample and the full sample. A similar picture is also suggested for the low- $z$  background.

<sup>1</sup> [https://github.com/esheldon/kmeans\\_radec](https://github.com/esheldon/kmeans_radec)



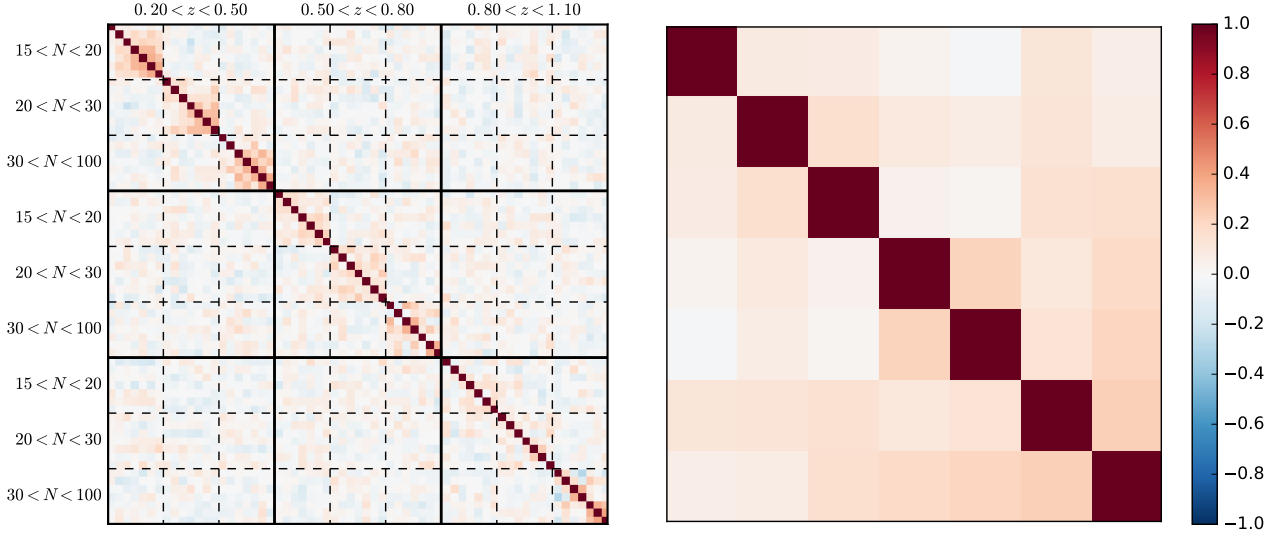


**Figure 9.** The correlation matrix of the magnification bias profiles for the high- $z$  background. The left panel shows the correlation matrix between different richness and redshift bins, where each box enclosed by the dashed (solid) lines represents the richness (redshift) bins indicated on the left y-axis (top x-axis). There is no significant correlation of the magnification bias between different richness and redshift bins. The right panel shows the correlation matrix derived by using all clusters without any richness and redshift binning.

**Table 1.** The summary of the parameters that are constrained in the scaling relation fitting. The first column records the names of the parameters. The second column shows the priors. The third to the fifth columns are the resulting constraints of the parameters using the low- $z$  high- $z$  and joint backgrounds, respectively. The sixth column presents the result including the two background populations of all clusters while applying the correction  $f_{\text{res}}(R)$  for the residual bias according to equation (24), in order to access the systematic uncertainty (see the text in Section 7). The seventh column is the result discarding the innermost radial bin, showing good agreement with our fiducial analysis.

Parameter	Priors	Constraints				
		Low- $z$	High- $z$	Joint	Joint Include all clusters with the $f_{\text{res}}$ correction	Joint Discard the innermost bin
$A_N$	(0, 100)	$18.33 \pm 10.22$	$21.13 \pm 3.69$	$19.63 \pm 3.16$	$24.20 \pm 4.15$	$19.76 \pm 3.86$
$B_N$	$\mathcal{N}(0.7, 0.2^2)$	$0.80 \pm 0.20$	$0.91 \pm 0.14$	$0.91 \pm 0.14$	$0.86 \pm 0.14$	$0.90 \pm 0.14$
$C_N$	$\mathcal{N}(0.0, 1^2)$	$-0.48 \pm 0.97$	$-0.25 \pm 0.75$	$-0.45 \pm 0.75$	$-0.14 \pm 0.74$	$0.20 \pm 0.78$
$\sigma_N$	$\mathcal{N}(0.15, 0.09^2)$ & (0.01, inf)	$0.16 \pm 0.08$	$0.15 \pm 0.08$	$0.14 \pm 0.07$	$0.14 \pm 0.07$	$0.16 \pm 0.08$
$\delta_{\text{low-}z}$	$\mathcal{N}(-0.0047, 0.0028^2)$	$-0.0060 \pm 0.0023$	...	$-0.0059 \pm 0.0022$	$-0.0032 \pm 0.0022$	$-0.0059 \pm 0.0022$
$\delta_{\text{high-}z}$	$\mathcal{N}(-0.0070, 0.0030^2)$	...	$-0.0049 \pm 0.0018$	$-0.0054 \pm 0.0018$	$-0.0034 \pm 0.0018$	$-0.0052 \pm 0.0019$

## 5.6 Modelling of the Scaling Relation

Our goal is to characterize the  $N$ - $M$  relation of the CAMIRA cluster sample using the HSC optical richness and weak-lensing magnification of individual clusters. To this end, we use a forward-modelling approach to constrain the richness-to-mass relation. Specifically, we assume an underlying  $N$ - $M$  relation characterized by its log-normal intrinsic scatter at fixed mass and evaluate the probability of observing the weak-lensing magnification signal for a given richness. This method has been widely used in previous work to calibrate the observable-to-mass relation of a cluster sample with a well-defined selection function (Chiu et al. 2016b; Chiu et al. 2018a; Bulbul et al. 2018). In addition, the effects of Malmquist and Eddington bias are fully accounted for in this approach. We have tested and validated the fitting procedure by using mock observations that are more than ten times larger than our clus-

ter sample. It is found that we can recover the true input parameters of the scaling relation within the  $1\sigma$  uncertainties. We describe our analysis framework below and refer the interested reader to Liu et al. (2015) and Bocquet et al. (2015) for more details.

For the  $i$ -th cluster at redshift  $z_i$  with the observed magnification profile  $\Delta\mu_i$  and the richness  $N_i$ , we evaluate the likelihood

$$\begin{aligned}
 \mathcal{L}(\Delta\mu_i | N_i, z_i, \mathbf{p}) &= \frac{P(\Delta\mu_i, N_i | z_i, \mathbf{p})}{P(N_i | z_i, \mathbf{p})} \\
 &= \frac{\int P(\Delta\mu_i, N_i | M_{500}, z_i, \mathbf{p}) n(M_{500}, z_i) dM_{500}}{\int P(N_i | M_{500}, z_i, \mathbf{p}) n(M_{500}, z_i) dM_{500}},
 \end{aligned} \tag{13}$$

where  $n(M_{500}, z_i)$  is the mass function at redshift  $z_i$ , and  $\mathbf{p}$  represents the parameter vector containing  $(A_N, B_N, C_N, \sigma_N)$  of the  $N$ - $M$

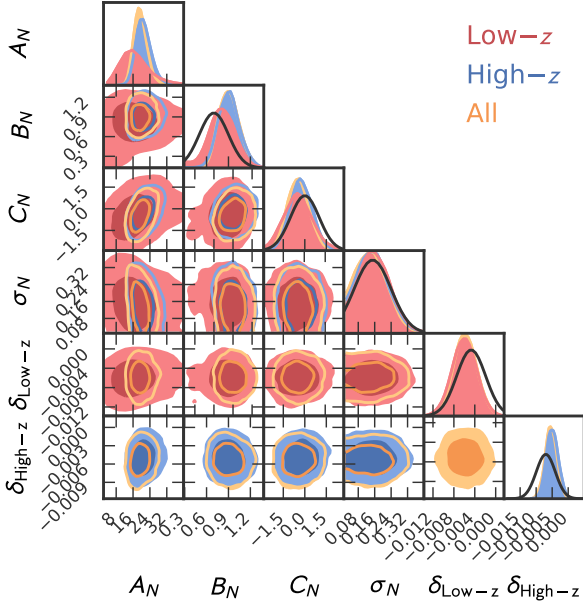


**Figure 10.** The constraints of the  $N$ – $M$  scaling relation parameters ( $A_N, B_N, C_N, \sigma_N$ ) and the marginalized global offsets ( $\delta_{\text{Low-}z}, \delta_{\text{High-}z}$ ). The red (blue) contours represent the  $1\sigma$  and  $2\sigma$  confidence levels for the low- $z$  (high- $z$ ) background. The resulting constraints of the low- $z$  and high- $z$  backgrounds are statistically consistent with each other, so we combine them to obtain the joint constraints, as shown by the yellow contours. The black curves are the adopted Gaussian priors on the parameters (see Table 1). We note that we additionally apply a hard cut on the lower bound of the intrinsic scatter parameter to ensure that  $\sigma_N > 0.01$ .

relation,

$$\langle \ln N | M_{500} \rangle = \ln A_N + B_N \ln \left( \frac{M_{500}}{M_{\text{piv}}} \right) + C_N \ln \left( \frac{1+z}{1+z_{\text{piv}}} \right), \quad (14)$$

with the log-normal intrinsic scatter at fixed mass of

$$\sigma_N \equiv \sigma_{\ln N | M_{500}}. \quad (15)$$

The pivot mass and redshift are fixed as  $M_{\text{piv}} = 10^{14} h^{-1} M_\odot$  and  $z_{\text{piv}} = 0.6$ , respectively. The inclusion of the mass function in equation (13) is necessary to account for the Eddington bias. Here we use the mass function of [Bocquet et al. \(2016\)](#).

The denominator of equation (13) represents the probability of obtaining the richness  $N_i$  for the  $i$ -th cluster at redshift  $z_i$  given the underlying mass  $M_{500}$  with the log-normal intrinsic scatter  $\sigma_N$  and the measurement uncertainty. The variance of the observed  $\ln(N)$  at fixed  $M_{500}$  can be expressed as

$$\text{Var}(\ln N | M_{500}) = \sigma_N^2 + \exp(-\langle \ln N | M_{500} \rangle), \quad (16)$$

where the second term is due to the Poisson noise. Hence, the  $P(N_i | M_{500}, z_i, \mathbf{p})$  term can be evaluated for a given parameter vector  $\mathbf{p}$ .

On the other hand, we can decompose the numerator of equation (13) as

$$P(\Delta\mu_i, N_i | M_{500}, z_i, \mathbf{p}) = P(\Delta\mu_i | M_{500}, z_i, \mathbf{p}) P(N_i | M_{500}, z_i, \mathbf{p}), \quad (17)$$

assuming that there is no correlated intrinsic scatter between  $\Delta\mu$  and  $N$ . This is a reasonable assumption because the magnification profile is derived using the background source sample behind clusters, which is independent of cluster member galaxies, to first order.

We evaluate the log-probability of the first term in equation (17) as

$$\ln P(\Delta\mu_i | M_{500}, z_i, \mathbf{p}) = -\frac{1}{2} (\Delta\mu_i - \Delta_{\text{model}i})^T \mathfrak{C}^{-1} (\Delta\mu_i - \Delta_{\text{model}i}), \quad (18)$$

where  $\mathfrak{C} = N_{i \in N-z \text{ bin}} \times \mathbb{C}$  is the covariance matrix in the richness-redshift bin which the  $i$ -th cluster belongs to (see Section 5.5), rescaled by the number  $N_{i \in N-z \text{ bin}}$  of clusters in that bin;  $\Delta_{\text{model}i}$  is the model prediction of the magnification profile for the  $i$ -th cluster with  $M_{500}$ . Specifically, the model prediction  $\Delta_{\text{model}i}$  at the projected radius  $R$  is expressed as

$$\Delta_{\text{model}i}(R) = \mu_i(R)^{\alpha-1} + \delta, \quad (19)$$

where the slope  $\alpha$  is fixed to the value at the magnitude cut  $m_{\text{cut}}$ . Additionally, we include one more free parameter  $\delta$  in our modelling to account for the global offset in our estimator caused by residual systematics in the bright-star mask correction, as we quantified using random field measurements (see Section 5.5). To evaluate  $\mu_i$ , we adopt the standard halo model ([Oguri & Hamana 2011](#)), which is a linear sum of a smoothly truncated version of the Navarro–Frenk–White (hereafter NFW; [Navarro et al. 1997](#)) profile and the 2-halo term:

$$\begin{aligned} \rho(r) &= f_t(r) \rho_{\text{NFW}}(r) + \rho_{2h}(r), \\ \rho_{\text{NFW}}(r) &= \frac{\rho_s}{(r/r_s)(1+r/r_s)^2}, \\ f_t(r) &= \left( \frac{1}{1 + \frac{r^2}{r_t^2}} \right)^2, \end{aligned} \quad (20)$$

where  $\rho_{\text{NFW}}(r)$  is the NFW density profile specified by the characteristic scale density  $\rho_s$  and the characteristic scale radius  $r_s$ , the transition term  $f_t(r)$  characterizes the steepening around a truncation radius,  $r_t$ , and the 2-halo term  $\rho_{2h}(r)$  is expressed as

$$\rho_{2h}(r) = \rho_m(z) b(M_{500}, z) \xi_m(r), \quad (21)$$

with  $b(M_{500}, z)$  the linear bias factor,  $\rho_m(z)$  the mean matter density of the universe evaluated at the cluster redshift, and  $\xi_m(r)$  the linear matter correlation function at the cluster redshift.<sup>2</sup> We set  $r_t = 4.5 R_{500}$ , which is consistent with the typical value used in the literature ([Oguri & Hamana 2011](#); [Umetsu et al. 2016](#)). We note that equation (20) reduces to the Baltz–Marchall–Oguri model ([Baltz et al. 2009](#)) when the 2-halo term is ignored.

We fix the concentration parameter of the NFW model and the linear bias factor  $b(M_{500}, z)$  to those predicted for the  $i$ -th cluster with  $M_{500}$  at the redshift  $z_i$  using the scaling relations of [Diemer & Kravtsov \(2015\)](#) and [Tinker et al. \(2010\)](#), respectively. Next, we calculate the surface mass density  $\Sigma_m(R)$  of the cluster at the projected radius  $R$  by integrating the mass density  $\rho(r)$  along the line of sight (i.e.,  $\Sigma_m(R) = \int \rho(\sqrt{R^2 + x^2}) dx$ ). Last, the mean lensing efficiency,  $\beta \equiv \int \frac{D_s}{D_s} P_f(z) dz$ , weighted by the stacked photometric redshift distribution  $P_f(z)$  of the source sample in the random field, is used to estimate the critical surface mass density  $\Sigma_c$ . That is, only one parameter—the cluster mass  $M_{500}$ —is needed to compute the model  $\Delta_{\text{model}i}$  for the  $i$ -th cluster at the redshift  $z_i$ .

The final likelihood is the product of all clusters,

$$\mathcal{L}(\mathbf{p}) = \prod_{i=1}^{N_{\text{cl}}} \mathcal{L}(\Delta\mu_i | N_i, z_i, \mathbf{p}), \quad (22)$$

where  $N_{\text{cl}}$  is the number of clusters. We explore the parameter space

<sup>2</sup> We express the correlation function in physical length units.

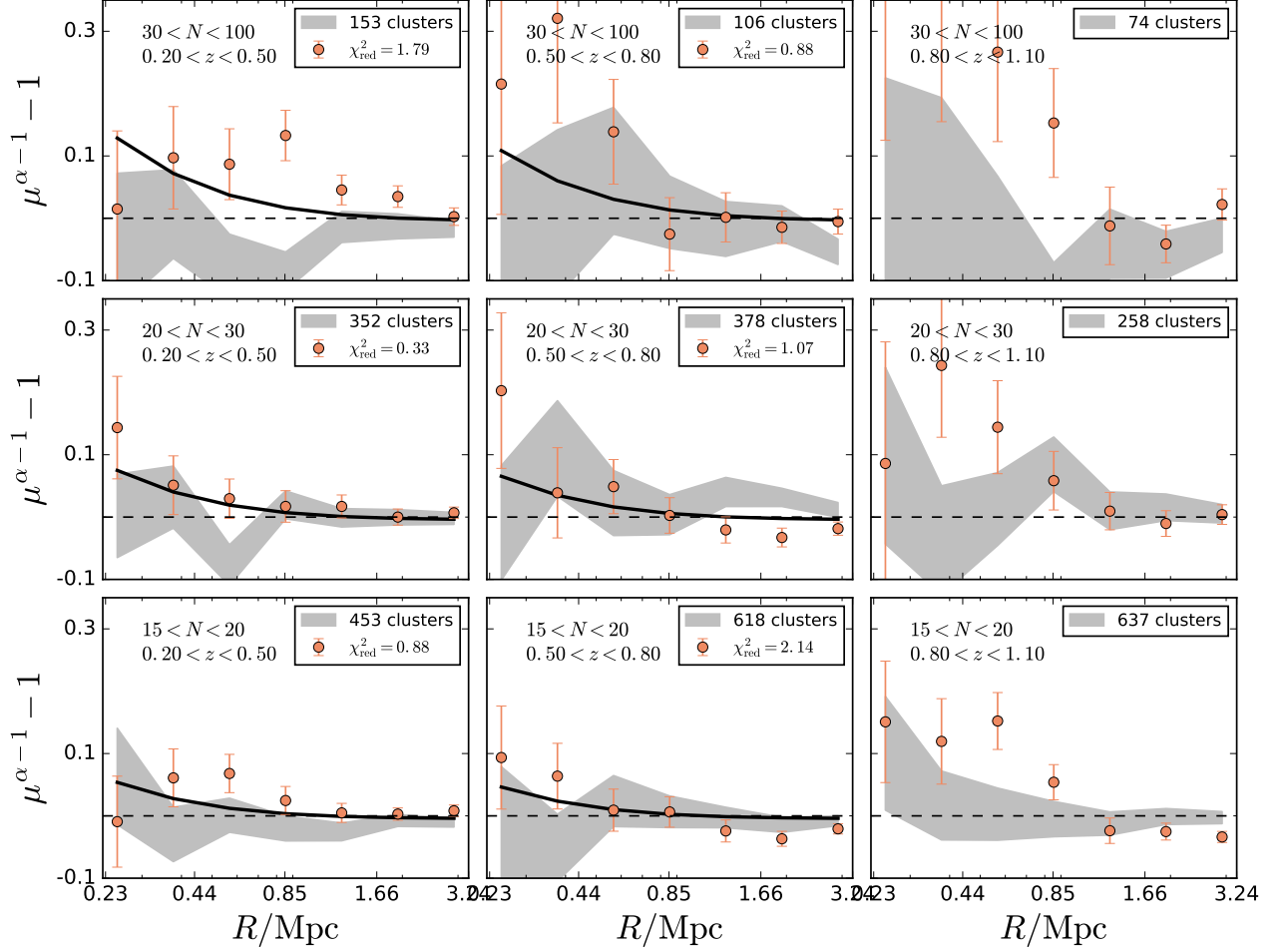


**Figure 11.** The stacked magnification bias profiles of the low- $z$  background in different richness and redshift bins. The  $x$ - and  $y$ -axis show the clustercentric radius in the physical unit and the magnification bias measurements, respectively. The data points are the stacked magnification profiles, while the black curves are the best-fit model predicted by using the joint constraints of the combined background. The grey area is the measurements by repeating the identical analysis on the random fields. The dashed lines indicate no signal of magnification bias. Each panel represents the result of the richness and redshift binning, for which the number of clusters used in the bin and the reduced chi-square with respect to the best-fit model are stated in the upper-right box. We note that we do not use the clusters at high redshift ( $0.8 < z < 1.1$ ) in fitting the magnification profiles derived from the low- $z$  background.

for our model using Bayesian inference in which the posterior probability distribution  $P(\mathbf{p})$  is expressed as

$$P(\mathbf{p}) = \mathcal{L}(\mathbf{p}) \cdot \mathcal{P}(\mathbf{p}), \quad (23)$$

where  $\mathcal{P}(\mathbf{p})$  is the prior probability distribution of the parameters  $\mathbf{p}$ . When analyzing the low- $z$  or high- $z$  background sample separately, we have five parameters in  $\mathbf{p}$ , namely the scaling relation parameters ( $A_N, B_N, C_N, \sigma_N$ ) and a parameter  $\delta$  describing the global offset of the estimator for each background sample (see Section 5.5). For a joint analysis of the combined low- $z$  and high- $z$  backgrounds, we have six parameters,  $\mathbf{p} = \{A_N, B_N, C_N, \sigma_N, \delta_{\text{low-}z}, \delta_{\text{high-}z}\}$ . We use *emcee* (Foreman-Mackey et al. 2013), the Python code employing the Affine Invariant Markov Chain Monte Carlo (MCMC) algorithm, to obtain the posterior probability distribution for our model parameters.

In this work, we cannot constrain the mass, redshift trends and

the log-normal intrinsic scatter using the current data alone. We thus focus on constraining the normalization parameter  $A_N$ , and adopt informative priors on  $B_N$ ,  $C_N$ , and  $\sigma_N$ . Specifically, a Gaussian prior of  $\mathcal{N}(0.7, 0.2^2)$  is applied on the mass trend parameter  $B_N$ . This prior is different from, but statistically consistent with, the previous results of Oguri (2014), Murata et al. (2018), and Murata et al. (2019). We assume a conservative Gaussian prior on the redshift trend parameter  $C_N$  of  $\mathcal{N}(0, 1^2)$  with a zero mean. We note that, according to previous studies (Saro et al. 2015; McClintock et al. 2019; Capasso et al. 2019b), we do not expect a strong dependence of richness on redshift at fixed mass. For the intrinsic scatter  $\sigma_N$ , we use the normal distribution  $\mathcal{N}(0.15, 0.09^2)$  suggested by Saro et al. (2015), with a lower bound of 0.01. We apply a uniform prior between 0 and 100 on the normalization  $A_N$ . The priors on  $\delta_{\text{low-}z}$  and  $\delta_{\text{high-}z}$  are taken to be  $\mathcal{N}(-0.0047, 0.0028^2)$  and  $\mathcal{N}(-0.0070, 0.0030^2)$ , respectively, which are based on our analy-

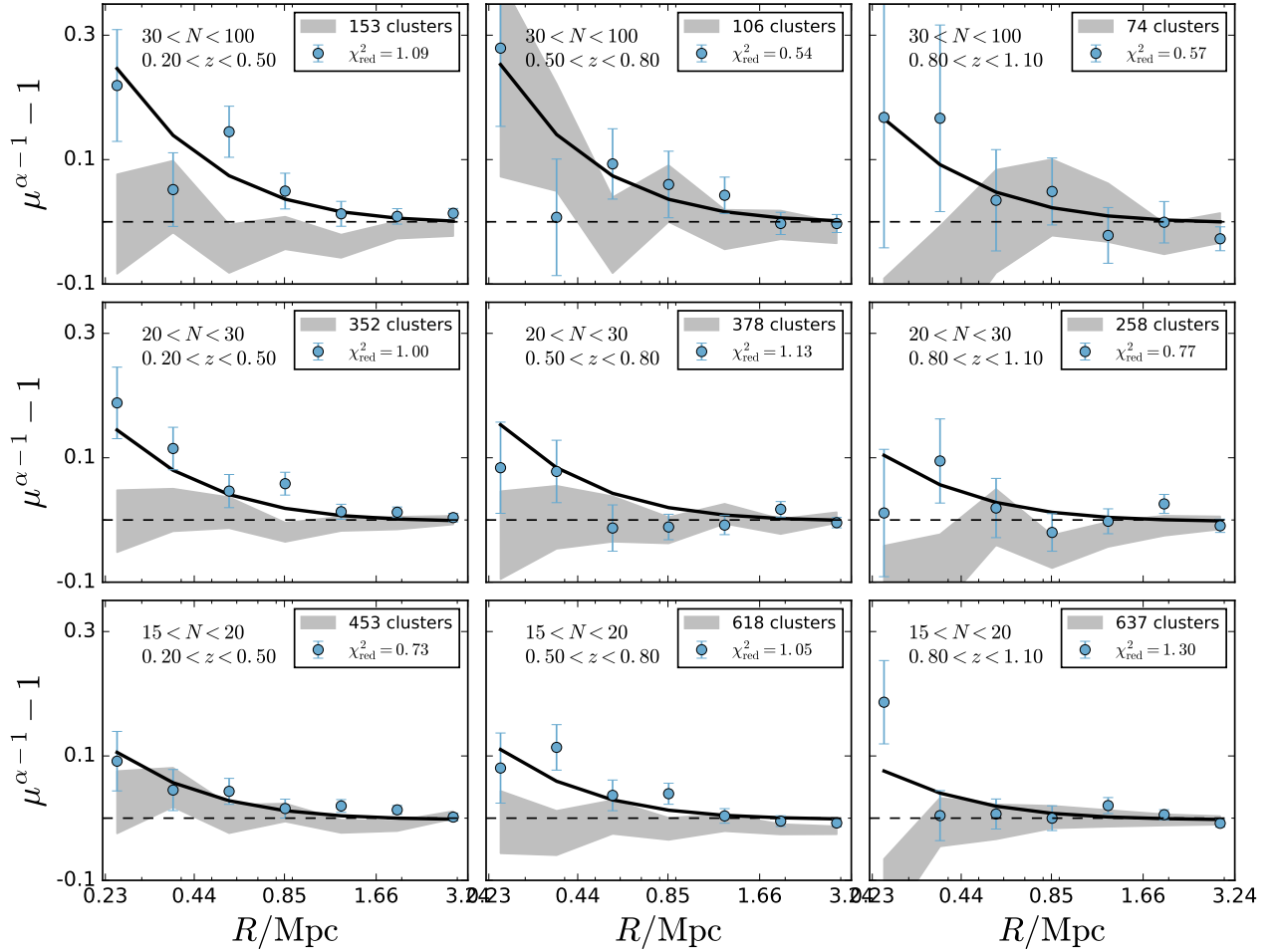


**Figure 12.** The stacked profile made in the same way as Figure 11 but for the case of the high- $z$  background.

sis of random fields (see Section 5.5). These priors are summarized in Table 1.

## 6 RESULTS AND DISCUSSION

In this section, we present and discuss the main results of this work, including the parameter constraints, the best-fit  $N$ – $M$  scaling relation, the stacked lensing profiles, and cluster mass estimates of individual clusters calibrated by weak lensing magnification.

In Section 5.6, we use a forward-modelling technique to simultaneously fit all individual clusters in our CAMIRA sample, effectively stacking all systems in the Bayesian likelihood space, and derive direct constraints on the parameters describing the  $N$ – $M$  scaling relation, namely  $(A_N, B_N, C_N, \sigma_N)$ . We first carry out the modelling for the low- $z$  and high- $z$  backgrounds separately. The results are summarized in Figure 10 and Table 1. We note that we can only constrain the normalization  $A_N$  of the scaling relation in this work, and the posterior distributions of the other parameters are mostly driven by the chosen priors. As seen in Figure 10, our constraint on  $A_N$  based on the low- $z$  background is in good agreement

with that on the high- $z$  background. Therefore, we can combine both low- $z$  and high- $z$  backgrounds to obtain joint constraints on the scaling relation, as shown in Figure 10. The resulting normalization  $A_N$  of the joint constraints is  $19.63 \pm 3.16$ , corresponding to an uncertainty at the level of 16%.

Next, we present the stacked profiles of lensing magnification bias. We stress again that we have simultaneously modeled all individual clusters in the likelihood space, so that we show the stacked lensing profiles here for visualization purposes only. Since we predict magnification profiles for all individual clusters in each sampled point of the parameter space, we can stack the best-fit profile of each individual cluster in data space. The stacked lensing magnification profiles of the low- $z$  background in different richness and redshift bins are presented in Figure 11, where the data points represent the stacked lensing measurements (see Section 5.5). Similarly, Figure 12 shows the results for the high- $z$  background. As seen in these figures, we find broad agreement between the stacked measurements and model predictions.

Furthermore, we stack all clusters together without richness and redshift binning. Since the covariance matrix depends on



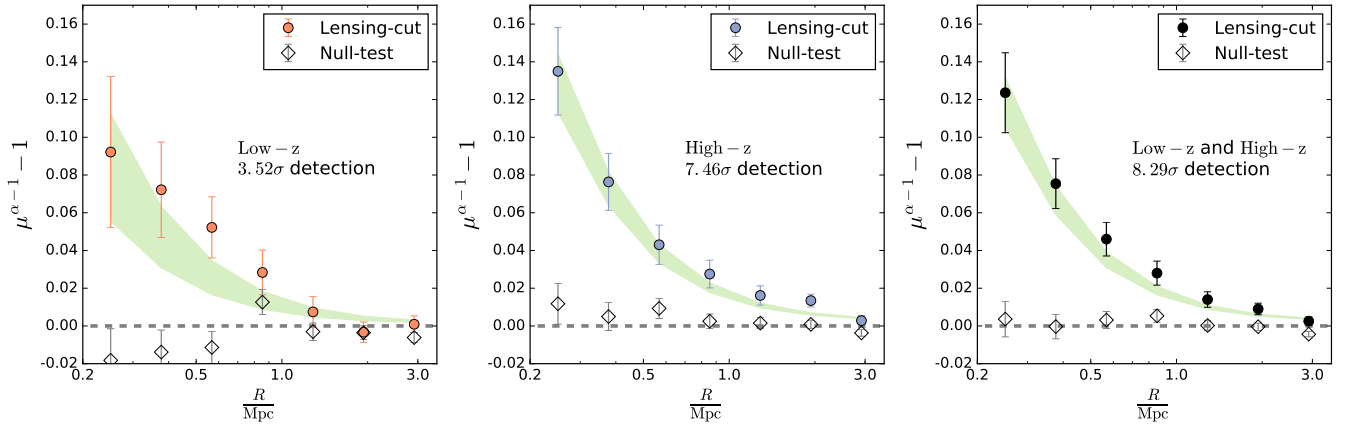


**Figure 13.** The stacked magnification profiles of low- $z$  (left), high- $z$  (middle) and the joint (right) backgrounds. The circles are the stacked profiles of the “lensing-cut” samples, showing the detection significance labelled in each plot. On the other hand, the open diamonds are the “null-test” samples, which are used to validate the magnification measurements and quantify the residual bias  $f_{\text{res}}$ ; they are all statistically consistent with zero. The green shaded regions in the left, middle and right panels, are the best-fit with the  $1\sigma$  confidence level using the low- $z$ , high- $z$  and the joint backgrounds, respectively.

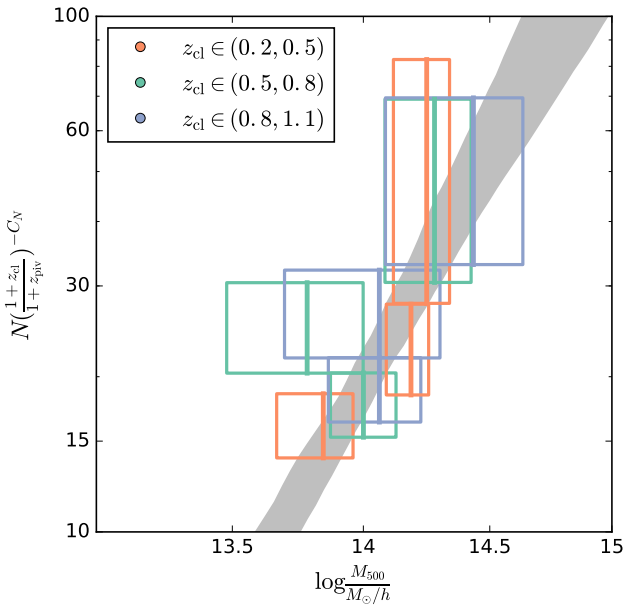


**Figure 14.** The stacked mass estimates of different richness-redshift bins and the resulting  $N$ – $M$  scaling relation of the CAMIRA clusters. The stacked mass in each richness and redshift bin is derived using the constraints of the combined background and is color-coded by the redshift as shown in the figure. The central and vertical line in each box indicates the peak location of the stacked mass probability distribution  $P(M_{500})$ , while the horizontal width of the box indicate the lower and upper 68% confidence limits (see Section 6). The range of the box in the y-axis represents the range of the richness of the clusters in the bin, normalized to the pivot redshift  $z_{\text{piv}}$ . The best-fit scaling relation is obtained by marginalizing all parameters constrained by the combined background, as shown in grey.

the cluster properties and the background source populations, we weight the magnification profiles of individual clusters by  $\tilde{w}$ . The weighting vector  $\tilde{w}$  is defined as the inverse of the diagonal part of the covariance matrix of each cluster. That is,  $\tilde{w} \equiv 1/\text{diag}(C_{i,b})$ , where  $i$  runs over all clusters, and  $b$  runs over the background pop-

ulations, namely the low- $z$  and high- $z$  backgrounds. We thus ignore the off-diagonal terms of the covariance matrix here for simplicity.

The resulting magnification profiles of the low- $z$  and high- $z$  backgrounds are presented in the left and middle panels of Figure 13, respectively. In the left and middle panels, we overplot the best-fit model profiles for the low- $z$  and high- $z$  backgrounds with their respective  $1\sigma$  confidence range (green shaded regions). The significance levels of detection after stacking are  $3.52\sigma$  and  $7.46\sigma$  for the low- $z$  and high- $z$  backgrounds, respectively.

We also stack the low- $z$  and high- $z$  backgrounds together to derive the combined stacked profile of magnification bias, as shown in the right panel of Figure 13. In total, stacking the low- $z$  and high- $z$  backgrounds for all 3029 clusters yields a detection significance level of  $8.29\sigma$ . As shown in Figure 13, the best-fit models provide reasonably good fits to the observed magnification measurements. We also overplot the stacked results of the “null-test” samples in Figure 13, showing that they are all statistically consistent with zero (i.e., no residual deviations).

In Figure 14 we summarize our results in the richness–mass space. Here the grey shaded area represents the joint constraints from the combined low- $z$  and high- $z$  background populations, marginalized over all parameters at the pivot redshift  $z_{\text{piv}}$ . The open boxes color-coded by the cluster redshift show the binned stacked constraints in different richness and mass bins. To be more exact, the stacked mass probability distribution  $P(M_{500})$  in each richness and redshift bin is obtained by computing the joint probability distribution of equation (18) for all clusters in that bin as a function of  $M_{500}$ . A clear positive correlation between the richness and cluster mass can be seen in Figure 14, albeit with large scatter. This  $N$ – $M$  relation exhibits little redshift dependence, as we quantified in this work ( $C_N = -0.45 \pm 0.75$ ). As shown in Figures 11–14, our results clearly demonstrate that we obtain significant constraints on the underlying  $N$ – $M$  scaling relation by stacking a large sample of clusters together, although each individual cluster measurement is noisy. In this work, we determine the normalization parameter  $A_N$  to a 16% precision.

Once we determine the underlying  $N$ – $M$  scaling relation, we can infer a lensing-calibrated estimate of  $M_{500}$  for each cluster using its observed richness in an ensemble manner. Specifically, we derive the probability distribution  $P(M_{500}|N, z)$  of  $M_{500}$  given the

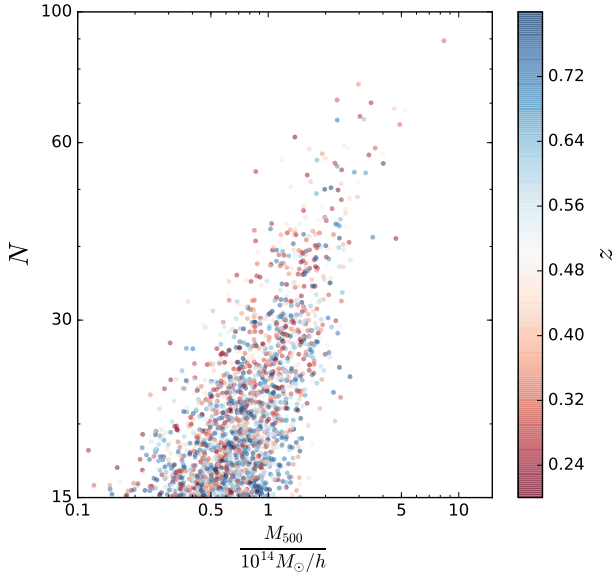


**Figure 15.** The observed richness  $N$  and richness-inferred mass  $M_{500}$  of individual clusters color-coded by the redshift as shown in the colorbar. Each cluster mass is sampled from the posterior of the mass distribution marginalizing over the all parameters (see the text in Section 6).

observed richness  $N$  at redshift  $z$  as

$$P(M_{500}|N, z, \mathbf{p}) \propto P(N|M_{500}, z, \mathbf{p})P(M_{500}|z, \mathbf{p}),$$

using the Bayes' theorem. Here we evaluate the second term  $P(M_{500}|z, \mathbf{p})$  using the halo mass function. Next, we randomly draw 500 realizations of the parameters  $\mathbf{p}$  from the MCMC-sampled posterior distributions and derive the probability distribution of  $M_{500}$  for each cluster given the richness and redshift. We use the posterior distributions from the joint low- $z$  and high- $z$  background constraints. In this way, we construct  $P(M_{500}|N, z)$  for each cluster while effectively marginalizing over all parameters. Finally, we randomly sample the value of  $M_{500}$  for each cluster from their resulting  $P(M_{500}|N, z)$ . This approach has been widely used in previous work (e.g., [Chiu et al. 2018a](#)), which demonstrates a statistically robust method for inferring individual cluster masses from ensemble population modeling ([Bocquet et al. 2018](#)).

The results are shown in Figure 15, where the richness-inferred mass of each cluster is plotted with their redshift color-coded. For clusters with  $N = 40$  and  $20$ , the average fractional uncertainty in  $M_{500}$  is  $\approx 30\%$  and  $\approx 38\%$ , respectively, after marginalizing over all parameters of the  $N$ – $M$  relation. If the parameters of the scaling relation are fixed to the best-fit values in Table 1—which means that we only consider the measurement uncertainty in richness and the intrinsic scatter—then the average fractional uncertainty of  $M_{500}$  is reduced to  $\approx 27\%$  and  $\approx 34\%$  at  $N = 40$  and  $20$ , respectively.

### 6.1 Comparison with previous work

Here we compare our derived  $N$ – $M$  relation of the CAMIRA sample to that of [Murata et al. \(2019\)](#) evaluated at the pivot redshift  $z_{\text{piv}}$ . [Murata et al. \(2019\)](#) independently determined the  $N$ – $M$  scaling relation of the CAMIRA sample in a forward-modeling approach by combining the HSC shear measurements and the CAMIRA cluster counts. Their analysis is based on the HSC first-year data covering

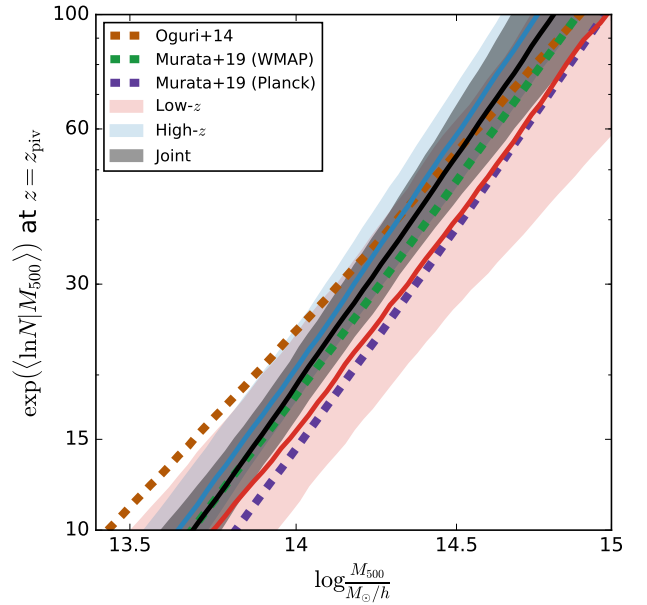


**Figure 16.** The comparison of the  $N$ – $M$  relations of the CAMIRA clusters at the pivot redshift  $z_{\text{piv}}$ . The results of this work based on the magnification bias using the low- $z$ , high- $z$  and the combined backgrounds are in red, blue and black, respectively. The 68% confidence levels, marginalizing over all other parameters, are all shown by the same color for each result. The  $N$ – $M$  relations of the CAMIRA clusters from [Murata et al. \(2019\)](#)—using the joint constraints of the weak lensing shearing effect and cluster number counts—are in green and purple under the cosmology with the cosmological parameters fixed to the *WMAP* and *Planck* results, respectively. Using a sample of CAMIRA clusters constructed by the SDSS data at  $0.1 < z < 0.3$ , the resulting  $N$ – $M$  relation from [Oguri \(2014\)](#) is shown in brown.

a smaller area of  $\approx 140 \text{ deg}^2$ . Their cluster sample spans similar ranges of mass and redshift to our study, thus providing an interesting comparison.

To this end, we first translate the cluster mass definition ( $M_{200\text{m}}$ ) adopted by [Murata et al. \(2019\)](#) into  $M_{500}$  by assuming an NFW density profile with the concentration parameter fixed to  $c_{500} \equiv R_{500}/r_s = 2.4$ , which is predicted by the [Diemer & Kravtsov \(2015\)](#)  $c$ – $M$  relation at the pivot mass  $M_{\text{piv}}$  and redshift  $z_{\text{piv}}$ . The results are shown in Figure 16. At  $M_{500} = 10^{14} h^{-1} M_{\odot}$ , the corresponding normalization of the  $N$ – $M$  relation of [Murata et al. \(2019\)](#) is 17.4 and 13.7 when using the mass slope of  $B_N = 0.83 \pm 0.03$  and  $0.86 \pm 0.05$  for their reference *WMAP* and *Planck* cosmology, respectively. Our constraint on  $A_N$  yields  $A_N = 18.33 \pm 10.22$  ( $21.13 \pm 3.69$ , or  $19.63 \pm 3.16$ ) according to the low- $z$  (high- $z$ , or combined) background-based results. That is, our magnification-based results are in good agreement with the shear-based ones of [Murata et al. \(2019\)](#) obtained assuming the *WMAP* cosmology. However, their results assuming the *Planck* cosmology are  $\approx 2\sigma$  discrepant with our results. Much larger samples are thus needed to further investigate the cause of this discrepancy. It is worth mentioning that using the weak shear effect alone cannot constrain well the mass and redshift trends either, as shown in [Murata et al. \(2019\)](#). This suggests that a joint analysis of weak-lensing and additional complementary probes is needed to obtain an adequate constraint on the  $N$ – $M$  scaling relation.

We also compare our results with [Oguri \(2014\)](#), who used weak lensing shear to constrain the mass-to-richness relation for

the CAMIRA sample at  $0.1 < z < 0.3$  using Sloan Digital Sky Survey (SDSS) data. A notable difference between our approach and theirs is that [Oguri \(2014\)](#) constructed the mass-to-richness relation, i.e.,  $P(M|N)$ , as opposed to the  $N$ - $M$  relation,  $P(N|M)$ , studied in this work. Therefore, we need to translate their constraints to  $P(N|M)$  for a fair comparison. Specifically, we use an analytic model described in [Evrad et al. \(2014\)](#) to translate their  $P(M|N)$  to  $P(N|M)$ , by accounting for the effect of intrinsic scatter. In short, this conversion requires the richness distribution and the intrinsic scatter in richness at fixed mass. Here we rely on the abundance analysis of [Murata et al. \(2019\)](#) for the former, and we approximate the latter by the best-fit value of  $\sigma_N$  obtained in this work. We translate  $P(M|N)$  of [Oguri \(2014\)](#) to  $P(N|M)$  at their pivot richness and redshift, and convert their virial mass definition to  $M_{500}$  by assuming an NFW profile with  $c_{500} = 2.4$ . The resulting constraints of [Oguri \(2014\)](#) are shown by the brown line in Figure 16. As seen in Figure 16, their results are in good agreement with ours within the errors, suggesting  $M_{500} \approx 10^{14} h^{-1} M_{\odot}$  at  $N \approx 20$ .

## 7 SYSTEMATICS

Here we discuss and quantify potential systematics that could bias our results.

In this work, the magnification signal has been measured from the projected number density contrast of background source samples with respect to random fields, accounting for the known bias from the cluster contamination and masking effects. We have quantified the level of residual bias by repeating the measurements using the “null-test” samples. It is important to stress that the residual bias correction  $f_{\text{res}}$  accounts for various systematics that could arise from, for example, the impact of any incorrect assumptions about the  $P(z)$ -decomposition and the deblending effect in the central cluster regions. However, it is likely that the primary source of residual bias is due to systematics in the photometry in the crowded fields, as discussed in Section 5.4. A detailed investigation with extensive simulations and dedicated spectroscopic follow-up observations is required to further clarify the cause of this residual bias.

In this work, we rely on an empirical approach to further quantify the impact of the residual bias on our final results. Specifically, we repeat the whole analysis assuming the residual residual bias  $f_{\text{res}}(R)$  in our measurements, by replacing equation (19) with the following:

$$\Delta\mu(R) = (\omega(R) + 1) \times \left( \frac{1 - f_{\text{cl}}(R)}{f_{\text{res}}(R)} \right) f_{\text{mask}}(R) - 1. \quad (24)$$

That is, we effectively calibrate the magnification signal of the “lensing-cut” samples against the “null-test” samples, assuming that these two samples share the same systematic errors due to the presence of the clusters. Using equation (24), we find that the resulting constraints on the parameters ( $A_N, B_N, C_N, \sigma_N$ ) from a joint fit to the combined background population<sup>3</sup> are  $(23.89 \pm 4.23, 0.85 \pm 0.14, -0.18 \pm 0.74, 0.15 \pm 0.08)$ , consistent with our fiducial analysis.

Assuming that applying the  $f_{\text{res}}$  correction can empirically remove the bias present in our magnification measurements of the low- $z$  background for the high-redshift clusters ( $0.8 \leq z < 1.1$ ), we could further include these measurements into our analysis. This results in parameter constraints of  $(A_N, B_N, C_N, \sigma_N) =$

$(24.20 \pm 4.15, 0.86 \pm 0.14, -0.14 \pm 0.74, 0.14 \pm 0.07)$ , as also tabulated in Table 1. That is, the inclusion of the high-redshift clusters at  $0.8 \leq z < 1.1$  in the fitting does not significantly change the resulting scaling relation, if the correction  $f_{\text{res}}$  is applied. Compared to our fiducial analysis, the most significant change in the parameter constraints is in the normalization  $A_N$ , which corresponds to a positive shift in  $A_N$  (or a negative offset in the mass  $M_{500}$ ) of  $0.8\sigma$ . To summarize, the residual bias in the “null-test” samples is the most important source of systematics, and the systematic changes in the parameters due to the residual bias correction can be regarded as systematic uncertainties in the present study.

We also estimate the level of potential bias due to systematic errors in the photometric redshift distribution, because a biased estimate of  $P(z)$  alters the lensing efficiency  $\beta$  and the cluster mass estimate. Specifically, we adopt a conservative value for the photo- $z$  bias  $|(z_{\text{phot}} - z_{\text{spec}})/(1 + z_{\text{phot}})|$  as estimated in [Tanaka et al. \(2018\)](#), shift the  $P(z)$  distribution by this amount, and estimate the resulting change in the cluster mass given the observed lensing signal. The photo- $z$  bias  $|(z_{\text{phot}} - z_{\text{spec}})/(1 + z_{\text{phot}})|$  is quantified by [Tanaka et al. \(2018\)](#) to be  $\delta z < 0.0005$  and  $0.007$  for the low- $z$  and high- $z$  backgrounds, respectively. Given a fixed magnification observable  $\omega$ , the inferred cluster mass is inversely proportional to  $\beta$  (see equation (2)). As a result, a shift of  $\delta z < 0.0005$  ( $0.007$ ) in  $P(z)$  leads to a change in mass of  $\lesssim 1\%$  ( $\approx 3\%$ ) for a cluster at  $z = 1.1$  when using the low- $z$  (high- $z$ ) background. In addition, this change decreases with decreasing cluster redshift. That is, this effect is negligible in this work.

In this work, we have ignored systematic uncertainties due to the projection effect ([Costanzi et al. 2019](#)), the triaxiality of clusters ([Chiu et al. 2018b](#)), the orientation bias ([Dietrich et al. 2014](#)), the presence of ICL ([Gruen et al. 2018](#)), the miscentering of clusters ([Ford et al. 2014](#)), the halo-modelling systematics ([Dietrich et al. 2019](#)), and the intrinsic scatter in the concentration-to-mass and the halo bias-to-mass relations. Given the current size of the statistical uncertainty, we expect the systematic errors above to be subdominant in this work.

## 8 SUMMARY AND CONCLUSIONS

In this paper, we have detected the density enhancement of background source galaxies due to lensing magnification around a sample of 3029 galaxy clusters with richness  $N > 15$  at  $0.2 \leq z < 1.1$ , which are optically selected in the Subaru HSC survey over the area of  $\approx 380 \text{ deg}^2$ . The lensing magnification effect is measured by using two distinct populations of low- $z$  and high- $z$  background galaxies at mean redshifts of  $\langle z \rangle \approx 1.1$  and  $\langle z \rangle \approx 1.4$ , respectively. We carefully correct for contamination by cluster members and the masking effect due to bright objects. Our magnification measurements are found to be uncontaminated according to validation tests based on the “null-test” samples, for which the net magnification effect is expected to vanish. The magnification bias effect has been detected at a significance level of  $3.52\sigma$ ,  $7.46\sigma$ , and  $8.29\sigma$  for the low- $z$ , high- $z$  and combined background sample, respectively.

With the constraints from lensing magnification alone, we use a forward-modelling approach to constrain the underlying  $N$ - $M$  scaling relation, which we characterize by a power-law relation described by four parameters: the normalization  $A_N$ , the mass-trend parameter  $B_N$ , the redshift-trend parameter  $C_N$ , and the log-normal intrinsic scatter  $\sigma_N$ . In this work, we can only constrain the normalization  $A_N$ , with an aid of informative priors on  $B_N$ ,  $C_N$  and  $\sigma_N$ . The  $A_N$  parameter is constrained by the low- $z$  and high- $z$  back-

<sup>3</sup> We note that we still discard the clusters at  $0.8 \leq z < 1.1$  for the low- $z$  background.

ground populations separately as  $18.33 \pm 10.22$  and  $21.13 \pm 3.69$ , respectively, at the pivot mass  $M_{\text{piv}} = 10^{14} h^{-1} M_{\odot}$ . Given this consistency between the measurements with the low- $z$  and high- $z$  backgrounds, we combine them together to derive an improved joint constraint. Using the combined background population, the resulting best-fit parameter  $A_N$  is  $19.63 \pm 3.16$  with a 16% uncertainty at the pivot mass.

With the derived  $N$ - $M$  scaling relation, we infer lensing-calibrated mass estimates for individual clusters based on the measured richness in an ensemble manner. At the characteristic richness of  $N \approx 40$  ( $\approx 20$ ), the fractional uncertainty in mass constrained by the combined background population is  $\approx 30\%$  ( $\approx 38\%$ ) when marginalizing over all parameters.

We find that the most significant source of systematic errors in this work is the residual bias found with the “null-test” samples. The source of residual bias is likely coming from systematics in the photometry in the crowded fields, which could result in biased estimates of colors and thus photo- $z$ , misidentification between cluster members and background galaxies, or the combination of both. A further investigation with intensive image simulations and spectroscopic follow-up observations of these clusters is needed to understand the cause of residual systematics. With the residual correction applied, the resulting normalization  $A_N$  from the combined background constraints increases at a significance level of  $0.8\sigma$ , suggesting a smaller mass scale at fixed richness compared to our fiducial results.

We compared our magnification-based constraints on the  $N$ - $M$  relation for the CAMIRA sample with the shear-based results of [Murata et al. \(2019\)](#) and [Oguri \(2014\)](#), finding that our normalization is in good agreement with their results. The comparison with [Murata et al. \(2019\)](#), who studied a subset of our CAMIRA sample, shows that our magnification-based  $N$ - $M$  relation is statistically consistent with their shear-based results obtained assuming the *WMAP* cosmology. However, the normalization of our magnification-based  $N$ - $M$  relation is higher at  $\approx 2\sigma$  than their shear-based one obtained assuming the *Planck* cosmology. This discrepancy arises because [Murata et al. \(2019\)](#) included the cluster abundance as a constraint into their shear-based weak-lensing analysis. A possible explanation for this discrepancy includes the redshift-dependent intrinsic scatter of richness at fixed mass, as proposed in [Murata et al. \(2019\)](#).

In this work, we have demonstrated that the cluster mass scale can be robustly inferred from lensing magnification alone, using well-calibrated deep multi-band photometry across the sky. Lensing magnification provides an independent way to calibrate an observable-to-mass scaling relation via gravitational lensing, and serves as a unique mass probe complementary to weak lensing shear, CMB lensing, and galaxy kinematics. One of the most important tasks to carry out such a magnification analysis is to select a clean sample of background galaxies at sufficiently high redshift, with a very low level of contamination. A possible improvement in future is to include near-Infrared data to select higher-redshift background populations ([Schrabback et al. 2018](#)). With the whole HSC-Wide coverage ( $\approx 1400 \text{ deg}^2$ ), we expect that the normalization of the  $N$ - $M$  relation could be determined to better than 8% precision, which will allow us to place competitive cosmological constraints using galaxy clusters.

## ACKNOWLEDGMENTS

I-Non Chiu acknowledges fruitful discussions during an international meeting entitled “Cosmology with size and flux magnification” held at the International Space Science Institute (ISSI), which was organized by Alan Heavens and Hendrik Hildebrandt. This work is supported by the Ministry of Science and Technology of Taiwan (grant MOST 106-2628-M-001-003-MY3) and by Academia Sinica (grant AS-IA-107-M01).

The Hyper Suprime-Cam (HSC) collaboration includes the astronomical communities of Japan and Taiwan, and Princeton University. The HSC instrumentation and software were developed by the National Astronomical Observatory of Japan (NAOJ), the Kavli Institute for the Physics and Mathematics of the Universe (Kavli IPMU), the University of Tokyo, the High Energy Accelerator Research Organization (KEK), the Academia Sinica Institute for Astronomy and Astrophysics in Taiwan (ASIAA), and Princeton University. Funding was contributed by the FIRST program from Japanese Cabinet Office, the Ministry of Education, Culture, Sports, Science and Technology (MEXT), the Japan Society for the Promotion of Science (JSPS), Japan Science and Technology Agency (JST), the Toray Science Foundation, NAOJ, Kavli IPMU, KEK, ASIAA, and Princeton University.

The Pan-STARRS1 Surveys (PS1) have been made possible through contributions of the Institute for Astronomy, the University of Hawaii, the Pan-STARRS Project Office, the Max-Planck Society and its participating institutes, the Max Planck Institute for Astronomy, Heidelberg and the Max Planck Institute for Extraterrestrial Physics, Garching, The Johns Hopkins University, Durham University, the University of Edinburgh, Queen’s University Belfast, the Harvard-Smithsonian Center for Astrophysics, the Las Cumbres Observatory Global Telescope Network Incorporated, the National Central University of Taiwan, the Space Telescope Science Institute, the National Aeronautics and Space Administration under Grant No. NNX08AR22G issued through the Planetary Science Division of the NASA Science Mission Directorate, the National Science Foundation under Grant No. AST-1238877, the University of Maryland, and Eotvos Lorand University (ELTE).

This paper makes use of software developed for the Large Synoptic Survey Telescope. We thank the LSST Project for making their code available as free software at <http://dm.lsst.org>. This work is based on data collected at the Subaru Telescope and retrieved from the HSC data archive system, which is operated by Subaru Telescope and Astronomy Data Center at National Astronomical Observatory of Japan.

This work made use of the IPython package ([Pérez & Granger 2007](#)), SciPy ([Jones et al. 2001](#)), TOPCAT, an interactive graphical viewer and editor for tabular data ([Taylor 2005](#)), matplotlib, a Python library for publication quality graphics ([Hunter 2007](#)), Astropy, a community-developed core Python package for Astronomy ([Astropy Collaboration et al. 2013](#)), NumPy ([Van Der Walt et al. 2011](#)). This work made use of [Bocquet & Carter \(2016\)](#) for producing Figure 10. This work made use of [colossus \(Diemer 2018\)](#) for calculating the cosmology-dependent quantities.

## APPENDIX A: CATALOG QUERY

In Table A1 we summarize the key `sql` statements to query the HSC database.



Flags			Meaning
isprimary	is	True	Select unique detection only
g[rizy]_pixelflags_edge	is	False	Discard the objects that are outside the usable exposure region
g[rizy]_pixelflags_interpolatedcenter	is	False	Discard the objects whose centers are flagged as interpolated
g[rizy]_pixelflags_crcenter	is	False	Discard the objects whose centers are flagged as cosmic ray
g[rizy]_cmodel_flag	is	False	Discard the objects whose final cmodel fits are failed
i[z]_pixelflags_bright_object	is	False	Discard the objects whose footprints contain a pixel flagged as star-masked
i_extendedness_value	==	1	Select galaxies only
g[r]countinputs	≥	4	Select full-depth in g and r-band
i[z]countinputs	≥	6	Select full-depth in i, z, and Y-band
z_cmodel_mag - a_z	<	26	Only use the objects with z-band magnitude brighter than 26 mag

**Table A1.** The sql query to construct the galaxy photometry catalog used in this work.**REFERENCES**

- Aihara H. et al., 2018a, PASJ, 70, S4  
Aihara H. et al., 2018b, PASJ, 70, S8  
Applegate D. et al., 2014, MNRAS, 439, 48  
Astropy Collaboration et al., 2013, A&A, 558, A33  
Axelrod T., Kantor J., Lupton R. H., Pierfederici F., 2010, in Proc. SPIE, Vol. 7740, Software and Cyberinfrastructure for Astronomy, p. 774015  
Baltz E. A., Marshall P., Oguri M., 2009, JCAP, 1, 015  
Bartelmann M., Schneider P., 2001, Physics Reports, 340, 291  
Baxter E. J. et al., 2018, MNRAS, 476, 2674  
Benson B. et al., 2013, ApJ, 763, 147  
Bocquet S., Carter F. W., 2016, 1  
Bocquet S. et al., 2018, arXiv e-prints, arXiv:1812.01679  
Bocquet S., Saro A., Dolag K., Mohr J., 2016, MNRAS, 456, 2361  
Bocquet S. et al., 2015, ApJ, 799, 214  
Bosch J. et al., 2018, PASJ, 70, S5  
Bridle S. et al., 2010, MNRAS, 405, 2044  
Broadhurst T., Taylor A., Peacock J., 1995, ApJ, 438, 49  
Bulbul E. et al., 2018, ArXiv e-prints  
Capak P. et al., 2007, ApJS, 172, 99  
Capasso R. et al., 2019a, MNRAS  
Capasso R. et al., 2019b, MNRAS, 482, 1043  
Chiu I., Desai S., Liu J., 2016, Astronomy and Computing, 16, 79  
Chiu I. et al., 2016a, MNRAS, 457, 3050  
Chiu I. et al., 2018a, MNRAS, 478, 3072  
Chiu I. et al., 2016b, MNRAS, 458, 379  
Chiu I.-N., Umetsu K., Sereno M., Ettori S., Meneghetti M., Merten J., Sayers J., Zitrin A., 2018b, ApJ, 860, 126  
Costanzi M. et al., 2019, MNRAS, 482, 490  
Coupon J., Czakon N., Bosch J., Komiyama Y., Medezinski E., Miyazaki S., Oguri M., 2018, PASJ, 70, S7  
de Haan T. et al., 2016, ApJ, 832, 95  
DES Collaboration, 2005, ArXiv Astrophysics e-prints  
Diemer B., 2018, ApJS, 239, 35  
Diemer B., Kravtsov A. V., 2015, ApJ, 799, 108  
Dietrich J. P. et al., 2019, MNRAS, 483, 2871  
Dietrich J. P. et al., 2014, MNRAS, 443, 1713  
Evrard A. E., Arnault P., Huterer D., Farahi A., 2014, MNRAS, 441, 3562  
Ford J., Hildebrandt H., Van Waerbeke L., Erben T., Laigle C., Milkeraitis M., Morrison C., 2014, MNRAS, 439, 3755  
Ford J. et al., 2012, ApJ, 754, 143  
Ford J., VanderPlas J., 2016, AJ, 152, 228  
Foreman-Mackey D., Hogg D., Lang D., Goodman J., 2013, PASP, 125, 306  
Grandis S., Mohr J. J., Dietrich J. P., Bocquet S., Saro A., Klein M., Paulus M., Capasso R., 2018, arXiv e-prints  
Gruen D. et al., 2014, MNRAS, 442, 1507  
Gruen D. et al., 2018, ArXiv e-prints  
Hartlap J., Simon P., Schneider P., 2007, A&A, 464, 399  
Hildebrandt H., Pielorz J., Erben T., van Waerbeke L., Simon P., Capak P., 2009, A&A, 498, 725  
Hoekstra H., Bartelmann M., Dahle H., Israel H., Limousin M., Meneghetti M., 2013, Space Science Reviews, 177, 75  
Hoekstra H., Herbonnet R., Muzzin A., Babul A., Mahdavi A., Viola M., Cacciato M., 2015, MNRAS, 449, 685  
Hoekstra H., Viola M., Herbonnet R., 2017, MNRAS, 468, 3295  
Holder G., Haiman Z., Mohr J., 2001, ApJ, 560, L111  
Hsieh B. C., Yee H. K. C., 2014, ApJ, 792, 102  
Huang S. et al., 2018, PASJ, 70, S6  
Hunter J. D., 2007, Computing In Science & Engineering, 9, 90  
Ilbert O. et al., 2009, ApJ, 690, 1236  
Ivezic Z. et al., 2008, Serbian Astronomical Journal, 176, 1  
Jones E., Oliphant T., Peterson P., et al., 2001, SciPy: Open source scientific tools for python  
Juric M., Tyson T., 2015, Highlights of Astronomy, 16, 675  
Lackner C. N., Gunn J. E., 2012, MNRAS, 421, 2277  
Lin Y.-T. et al., 2017, ApJ, 851, 139  
Liu J. et al., 2015, MNRAS, 448, 2085  
Lupton R., Gunn J. E., Ivezić Z., Knapp G. R., Kent S., 2001, in Astronomical Society of the Pacific Conference Series, Vol. 238, Astronomical Data Analysis Software and Systems X, Harnden Jr. F. R., Primini F. A., Payne H. E., eds., p. 269  
Mandelbaum R. et al., 2018, PASJ, 70, S25  
Mandelbaum R. et al., 2015, MNRAS, 450, 2963  
Mantz A. B. et al., 2015, MNRAS, 446, 2205  
Martino R., Mazzotta P., Bourdin H., Smith G., Bartalucci I., Marone D., Finoguenov A., Okabe N., 2014, ArXiv e-prints  
Massey R. et al., 2007, MNRAS, 376, 13  
McClintock T. et al., 2019, MNRAS, 482, 1352  
Medezinski E., Broadhurst T., Umetsu K., Oguri M., Rephaeli Y., Benítez N., 2010, MNRAS, 405, 257  
Medezinski E. et al., 2018, PASJ, 70, 30  
Melchior P. et al., 2017, MNRAS, 469, 4899  
Miyatake H. et al., 2019, ApJ, 875, 63  
Miyazaki S., 2015, IAU General Assembly, 22, 2255916  
Murata R., Nishimichi T., Takada M., Miyatake H., Shirasaki M., More S., Takahashi R., Osato K., 2018, ApJ, 854, 120  
Murata R. et al., 2019, arXiv e-prints, arXiv:1904.07524  
Navarro J., Frenk C., White S., 1997, ApJ, 490, 493  
Oguri M., 2014, MNRAS, 444, 147  
Oguri M., Hamana T., 2011, MNRAS, 414, 1851  
Oguri M. et al., 2018, PASJ, 70, S20  
Okabe N., Smith G. P., 2016, MNRAS, 461, 3794

- Pérez F., Granger B. E., 2007, *Computing in Science and Engineering*, 9, 21
- Planck Collaboration et al., 2015, *ArXiv e-prints*
- Polsterer K. L., D’Isanto A., Gieseke F., 2016, *ArXiv e-prints*
- Rowe B. et al., 2015, *Astronomy and Computing*, 10, 121
- Rykoff E. et al., 2012, *ApJ*, 746, 178
- Saro A. et al., 2015, *MNRAS*, 454, 2305
- Saro A., Mohr J., Bazin G., Dolag K., 2013, *ApJ*, 772, 47
- Schneider P., King L., Erben T., 2000, *A&A*, 353, 41
- Schrabback T. et al., 2018, *MNRAS*, 474, 2635
- Sereno M., Covone G., Izzo L., Ettori S., Coupon J., Lieu M., 2017, *MNRAS*, 472, 1946
- Stern C. et al., 2018, *ArXiv e-prints*
- Suchyta E. et al., 2016, *MNRAS*, 457, 786
- Tanaka M. et al., 2018, *PASJ*, 70, S9
- Taylor A., Dye S., Broadhurst T., Benitez N., van Kampen E., 1998, *ApJ*, 501, 539
- Taylor M. B., 2005, in *Astronomical Society of the Pacific Conference Series*, Vol. 347, *Astronomical Data Analysis Software and Systems XIV*, Shopbell P., Britton M., Ebert R., eds., p. 29
- Tinker J. L., Robertson B. E., Kravtsov A. V., Klypin A., Warren M. S., Yepes G., Gottlöber S., 2010, *ApJ*, 724, 878
- Tudorica A. et al., 2017, *A&A*, 608, A141
- Umetsu K., 2011, in *International School of Physics ‘Enrico Fermi’: Astrophysics of Galaxy Clusters*, Cavaliere A., Rephaeli Y., eds., Vol. 172, IOS Press, pp. 269–300
- Umetsu K., 2013, *ApJ*, 769, 13
- Umetsu K., Broadhurst T., 2008, *ApJ*, 684, 177
- Umetsu K., Broadhurst T., Zitrin A., Medezinski E., Hsu L.-Y., 2011, *ApJ*, 729, 127
- Umetsu K. et al., 2014, *ApJ*, 795, 163
- Umetsu K. et al., 2018, *ApJ*, 860, 104
- Umetsu K., Zitrin A., Gruen D., Merten J., Donahue M., Postman M., 2016, *ApJ*, 821, 116
- Van Der Walt S., Colbert S. C., Varoquaux G., 2011, *Computing in Science & Engineering*, 13, 22
- Varga T. N. et al., 2018, *arXiv e-prints*, arXiv:1812.05116
- Vikhlinin A. et al., 2009, *ApJ*, 692, 1033
- Vikhlinin A., Kravtsov A., Forman W., Jones C., Markevitch M., Murray S., Van Speybroeck L., 2006, *ApJ*, 640, 691
- von der Linden A. et al., 2014, *MNRAS*, 439, 2
- Wang L., Steinhardt P. J., 1998, *ApJ*, 508, 483